



Angela Bartel

Laboratory Scale Experiments on the Production of Precipitated Calcium Carbonate from Steelmaking Slag via Spray Carbonation

Master Thesis for the degree:

Nordic Master in Innovative Sustainable Energy Engineering, M.Sc. (Tech.)

Aalto University, Finland and Royal Institute of Technology, Sweden

Aalto University, Espoo, 27.03.2017

Supervisor: Mika Järvinen, Associate Professor, D.Sc. (Tech.)

Advisor: Arshe Said, M.Sc. (Tech)

Author Angela Bartel

Title of thesis Laboratory Scale Experiments on the Production of Precipitated Calcium Carbonate from Steelmaking Slag via Spray Carbonation

Degree programme Degree Programme in Energy Engineering and HVAC

Major Innovative Sustainable Energy Engineering**Code** IA3025

Thesis supervisor Mika Järvinen

Thesis advisor Arshe Said

Date 27.03.2017**Number of pages** 53 + 6**Language** English

Abstract

This study investigates a new concept of producing precipitated calcium carbonate (PCC) from steelmaking slag and carbon dioxide via a spray carbonation process. The presented laboratory-scale spray carbonation test reactor uses a spray nozzle to disperse fine droplets of a Ca-rich solution into a spray tower, where calcium carbonate precipitates as a result of the reaction between calcium and the counter flowing CO₂ gas. Beside the spray carbonation experiments with the laboratory-scale test plant, a spray analysis was conducted to determine the droplet size of different spray nozzles. This work also presents a comparison between the original X2PCC process and the proposed spray carbonation process and tries to identify its shortcomings and advantages.

The feasibility of PCC production from steel slag via spray carbonation was successfully demonstrated at the laboratory-scale. Experiments were conducted at pressures of 5 and 10 bar using nozzles with different capacities and spray angles. All experiments succeeded in producing PCC in the form of rhombohedral calcite with a size of 22.86 to 66.98 µm. The calcite content of the produced PCC was between 80.43 and 96.59 %.

Droplet collisions and depositions on the spray tower wall were found to play an important role when trying to produce PCC of a certain size. Experiments also show that it is possible to produce smaller PCC particles with the spray carbonation process compared to the conventional X2PCC process, which makes it a potential alternative and a promising research area in the future.

Keywords PCC, Precipitated Calcium Carbonate, Spray Carbonation, Steel Slag, Gas-Liquid Mass Transfer, Spray Analysis, Carbon Capture and Storage.

Acknowledgments

I would like to thank my supervisor Professor Mika Järvinen for giving me the opportunity to work on this thesis as part of the X2PCC project and for the valuable discussions and feedback. Great thanks to my advisor Arshe Said for all the support and valuable time spent with the experimental work.

I also want to acknowledge the great contribution of Vadim Desyatnyk and the other technical staff from the Department of Mechanical Engineering for setting up the test plant and for their technical support during the time of the thesis. Thanks to Tuomas Paloposki for sharing his knowledge about the Malvern particle analyser and support, without which the spray-analysis would not have been possible.

Last but not least thanks to Tuyen Nguyen from the Department of Chemical Technology for performing the PSD analysis and to Leena Palmu and Marcin Selent from the Oulu University for performing the morphology analyses.

Espoo, 27.03.2017

Angela Bartel

Angela Bartel

Contents

Acknowledgments	I
Contents	II
Nomenclature	III
List of Figures	V
List of Tables	VI
1 Introduction	1
1.1 Scope of Work.....	2
1.2 Research Objectives	2
2 Precipitated Calcium Carbonate (PCC)	3
2.1 Production of PCC	3
2.2 Applications of PCC	4
2.3 Morphology.....	5
3 Principles of PCC Precipitation	7
3.1 Mass Transfer between Gas and Liquid Phase	8
3.1.1 Two-film Model.....	9
3.1.2 Effect of Chemical Reactions on the Mass Transfer	10
3.1.3 Internal Circulation	14
3.1.4 Mass Transfer of the CO ₂ - Ca(OH) ₂ System.....	14
4 X2PCC Process	16
4.1 Main Findings from Previous Experimental Studies	17
4.1.1 Parameters Affecting Calcium Extraction Efficiency	18
4.1.2 Parameters Affecting Precipitation	18
5 Spray Carbonation	20
5.1 Spray Carbonation Process	20
5.1.1 Spray Nozzle.....	21
6 Experimental Work	26
6.1 Spray Analysis	26
6.1.1 Methodology	26
6.1.2 Results.....	27
6.1.3 Discussion.....	29
6.1.4 Calculations Based on Experimental Results	30
6.2 Spray Carbonation Experiments	31
6.2.1 Equipment Setup.....	31
6.2.2 Methodology	32
6.2.3 Results & Discussion	33
6.2.4 Experimental Learning and Challenges	42
7 Conclusion	45
8 Recommendations	46
References	48
Appendices	53

Nomenclature

Abbreviations

CCS	Carbon capture and storage
GCC	Ground calcium carbonate
G/L ratio	Gas-to-liquid ratio
GPH	Gallons per hour (1GPH = 3.785 L/h)
HV	Narrow spray pattern
N-L-D	Nozzle-to-laser beam distance
PCC	Precipitated calcium carbonate
PLP	Semi hollow spray pattern
PSD	Particle size distribution
R or S	Full cone spray pattern
SEM	Scanning Electron Microscope
SG	Specific gravity
SLR	Solid-to-liquid ratio
XRD	X-ray diffraction

Symbols

\hat{a}	Interfacial area, m^2/m^3
b	Stoichiometric coefficient of species B
C	Molar concentration, mol/m^3
C_D	Drag coefficient
d	Diameter, m
D	Diffusivity, m^2/s
$D(v, 0.5)$	Volume-based median diameter, m
E	Enhancement factor
E_∞	Infinite Enhancement factor
g	Gravitational force = $9.81 \text{ m}/\text{s}^2$
Ha	Hatta number
k	Reaction rate, $\text{mol}/\text{L}\cdot\text{s}$
k_H	Henry's law constant, $\text{Pa}\cdot\text{m}^3/\text{mol}$
k_L	Mass transfer coefficient, m/s
M	Diffusion-reaction parameter
N	Absorption flux, $\text{mol}/\text{m}^2\cdot\text{s}$
p	Pressure, Pa
Q	Flow rate, m^3/s
q	Relative abundance parameter
r	Radius, m
Re	Reynolds number
t	Time, s
u_d	Droplet velocity, m/s
u_g	Gas velocity, m/s
u_r	Relative velocity, m/s
u_{td}	Droplet's terminal velocity, m/s
V	Volume, m^3
x	Dimensionless distance

Greek letters

α, β, ζ	Dimensionless variables
δ	Film thickness, m
λ	Dimensionless distance
μ	Viscosity, Pa·s
ρ	Density, kg/m ³
σ	Surface tension, N/m

Subscripts

A	Species A
B	Species B
b	Liquid bulk
bub	Bubble
d	Droplet
g	Gas / Gas phase
gas	Gaseous
o	Orifice
s	Solid

Superscripts

*	at equilibrium
n	Flow exponent

Chemical Compounds

CaCl ₂	Calcium chloride
CaCO ₃	Calcium carbonate
CaO	Calcium oxide
Ca(OH) ₂	Calcium hydroxide / Slaked lime
CaSiO ₃	Calcium silicate
Ca ₂ SiO ₄	Larnite
CO ₂	Carbon dioxide
CO ₃	Carbonate
HCO ₃	Bicarbonate
H ₂ O	Water
Na ₂ CO ₃	Sodium carbonate
NaCl	Sodium chloride
NaOH	Sodium hydroxide
NH ₄ Cl	Ammonium chloride
(NH ₄) ₂ CO ₃	Ammonium carbonate
NH ₄ OH	Ammonium hydroxide / Aqueous ammonia
OH	Hydroxide

List of Figures

Figure 1: Global end-use market structure for PCC (2013) [12]	4
Figure 2: Scanning Electron Microscope pictures of a) rhombohedral calcite, b) aragonite and c) vaterite produced with the X2PCC process. [16]	5
Figure 3: Mass transfer of solute A across the gas-liquid interface	9
Figure 4: Concentration profiles of A and B in the liquid bulk under the slow reaction regime (adapted from [40])	13
Figure 5: Transition from fast reaction regime to instantaneous reaction regime.....	13
Figure 6: Droplet with relative gas-droplet motion and internal circulation [50].....	14
Figure 7: Simplified schematic of the X2PCC process.....	16
Figure 8: Simple schematic of the spray carbonation process	20
Figure 9: Nozzle spray patterns (Adapted from [68]).....	21
Figure 10: Main forces acting upon falling droplet [71].....	23
Figure 11: Droplet-gas interactions (Adapted from [75])	25
Figure 12: Typical experimental configuration for spraying tests with Malvern particle sizer [76]	26
Figure 13: Positioning of the Monarch 5.50 GPH 60° nozzle; left picture: 20 mm nozzle-to-laser beam distance; right picture: 40 mm nozzle-to-laser beam distance.....	27
Figure 14: Mean diameter and standard deviation of spray droplets of Monarch 5.50 GPH 60° at different water pressures measured at two different distances of the nozzle to the laser beam	28
Figure 15: Mean diameter of spray droplets from 7 different nozzles at different water pressures measured with Malvern particle sizer at a nozzle-to-laser beam distance of 4 cm.	28
Figure 16: Mean diameter of spray droplets from spray nozzles with full cone spray pattern at 5 bar water pressure measured with Malvern particle sizer at a nozzle-to-laser beam distance of 4 cm.	29
Figure 17: Spray tower and pressure tank of the laboratory-scale test plant	31
Figure 18: Result of PCC particle size measurements: mean particle size and standard deviation .	34
Figure 19: PSD of Test 5 (left) and Test 8 (right) before, with and after the application of ultrasound.....	35
Figure 20: Comparison of PSD (after ultrasound) between samples of spray carbonation tests (Test 2 and Test 8) and conventional X2PCC carbonation tests (Test 4 X2PCC and Test 9 X2PCC)	36
Figure 21: Comparison of droplet diameter, PCC particle size (after us) and theoretical PCC particle size (side length of cube-shaped particle)	36
Figure 22: Actual and theoretical PCC particle size vs. droplet size	37
Figure 23: Comparison of PCC particle size of spray carbonation tests with nozzles with same flow rate (5.50 GPH) but different spray angles (60°, 45°, and 30°).....	38
Figure 24: Comparison of PCC particle sizes of spray carbonation tests with DANFOSS nozzles with a spray angle of 45° and varying flow rates	38
Figure 25: Comparison of average PCC particle size ($D [v, 0.5]$ in μm) of spray carbonation tests with 5 and 10 bar.....	39
Figure 26: SEM images of samples from Test 1 (left) and Test 2 (right)	40
Figure 27: SEM images of samples from Test 4 (left) and Test 5 (right)	41
Figure 28: SEM images of samples from Test 6 (left) and Test 7 (right)	41
Figure 29: SEM images of samples from Test 8 (left) and Test 9 (right)	41
Figure 30: SEM images of samples from Test 10 (left) and Test 11 (right)	42
Figure 31: Picture showing dirt particles on the nozzle filter (1); PCC depositions on the Monarch 5.50 60° nozzle (2); oxidized DANFOSS 0.60 GPH 45° nozzle (3).....	43

List of Tables

Table 1: Main chemical reactions of the carbonation, Solvay and lime-soda process [6]	3
Table 2: Properties of commercial PCC products in the pulp & paper industry [2]	4
Table 3: Possible regimes for mass transfer accompanied by chemical reaction [39,43].....	12
Table 4: Selected nozzles for experimental work	21
Table 5: Estimated nozzle capacities for water and the Ca-rich solution at a spraying pressure of 5 bar.....	22
Table 6: Estimated stoichiometric volume flow of CO ₂ into the spray tower	22
Table 7: Recommended drag correlations; $w = \log_{10} Re$ [72]	24
Table 8: Correlation between terminal velocity and droplet diameter by the example of the Monarch 5.50 GPH 60° PLP nozzle.....	24
Table 9: Terminal velocity calculated for each nozzle based on the droplet size data obtained by the spray analysis (pressure = 5 bar)	30
Table 10: Theoretical particle size of a cube-shaped PCC particle (V=volume; s=cube's side length).....	30
Table 11: Key components of the laboratory-scale test plant	31
Table 12: Run matrix for the laboratory-scale spray carbonation experiments	32
Table 13: Results for the spray carbonation experiments	33
Table 14: Decrease of D (v, 0.9) particle size - compared before and after the application of ultrasound	35
Table 15: Results of the morphology analysis of samples from the spray carbonation experiments	40

1 Introduction

The accelerating release of human-caused emissions into the atmosphere has long passed the limit where existing CO₂ uptake mechanisms are able to offset these vast amounts of emissions. The need for action to combat climate change and reduce anthropogenic emissions has not only recently awakened the interest in carbon capture and storage (CCS) processes. Generally, the CCS scheme consists of three parts: CO₂ capture, transportation, and sequestration (long-term storage of carbon dioxide). Both carbon capture and sequestration are alternatives to reduce greenhouse gas emissions and mitigate climate change. Besides physical processes of carbon sequestration also chemical processes exist, one of them being mineral carbonation, also known as mineral sequestration. In mineral carbonation CO₂ reacts with magnesium or calcium containing silicate minerals to form insoluble and geologically stable carbonates. Hence, mineral carbonation not only provides a permanent storage of CO₂, but also yields precipitated calcium carbonate (PCC) which can be a valuable product if it meets certain quality criteria [1,2].

Because of their high contents of calcium silicates, slags from iron and steel works have been identified as potential raw materials for mineral carbonation. [3] Current production of PCC is based on the carbonation of mined limestone. In the carbonation process limestone is first heated to very high temperatures to produce lime, which is a very energy intensive step in lime production. According to a report by the European Lime Association [4] the amount of direct CO₂ emissions caused by fuel combustion for lime kiln heating of the European lime industry was equal to approx. 7.8 million tonnes in 2010. The amount of CO₂ emitted per tonne of lime produced ranged from 0.322 to 0.635 tonnes [5]. Replacing the energy intensive calcination process by using slag as a raw material instead, could considerably decrease energy consumption as well as carbon dioxide emissions. Reusing steelmaking slags instead of dumping them in disposal areas can furthermore prevent harmful impacts on both human health and the environment [6].

One recently studied mineral carbonation process for carbon capture is the X2PCC process, which uses an aqueous solution of ammonium chloride (NH₄Cl) to extract calcium from steelmaking slag. The resulting Ca-rich solution is fed into a carbonation reactor, where it reacts with CO₂ to form PCC. Provided that the produced PCC shows sufficient high quality, it can be sold to other industries e.g. as filler material in the paper making industry. Earlier work on the X2PCC process has not only focused on the extraction of calcium from steel slag, but also on the precipitation kinetics of PCC, as well as on economics and business aspects. Great emphasis was laid to study the impact of different precipitation factors on the quality of the PCC. With the successful operation of the pilot plant at the Aalto University an industrial scale demonstration plant is currently under construction.

1.1 Scope of Work

This work investigates a new concept of producing PCC from steelmaking slag and carbon dioxide, namely via a spray carbonation process. This idea was already presented in the patent [7] covering the calcium carbonate production method from waste and side products, and is now validated with this work. The research focuses on the differences between the original X2PCC process and the proposed spray carbonation process and investigates whether the concept of a spray carbonation process can be achieved. Furthermore, this work presents a laboratory-scale prototype which has been designed to determine the feasibility of the process and to identify its shortcomings and advantages.

First, a brief description of the production, application, and the morphology of PCC are given in Chapter 2. The principles of PCC precipitation are then explained in Chapter 3. A short introduction to the original X2PCC process is given in Chapter 4, while Chapter 5 presents the theoretical background on spray carbonation, including a description of the laboratory test rig. The experimental work of this research is described in Chapter 6. A final conclusion and recommendations for future work are given in Chapters 7 and 8 respectively. It shall be mentioned, that this work only focuses on the carbonation step and therefore no further experiments on the calcium extraction have been conducted. The Ca-rich solution is provided and produced via the conventional X2PCC process, using the pilot scale plant at the Aalto University.

1.2 Research Objectives

The main objective of this work is to verify the concept of producing precipitated calcium carbonate via spray carbonation. The main research question was, if it is possible to generate precipitated calcium carbonate via spray carbonation and what effects on particle morphology and particle size can be observed.

This thesis tries to answer following questions:

- How does the spray carbonation process differ from the original X2PCC process concept?
- Is it possible to generate PCC via spray carbonation?
- What is the impact of spray carbonation on particle morphology?
- How does the droplet size of the Ca-rich solution affect the chemical reaction and the PCC particle size?

2 Precipitated Calcium Carbonate (PCC)

Calcium carbonate (CaCO_3) is one of the most common minerals on earth and occurs naturally as limestone, chalk, and marble. [8] Ground calcium carbonate (GCC) is simply produced by grinding calcium carbonate deposits resulting in particles usually bigger than $1\mu\text{m}$. Precipitated calcium carbonate (PCC) on the contrary is a precipitate that is produced by the reaction of carbon dioxide (CO_2) with calcium hydroxide ($\text{Ca}(\text{OH})_2$). PCC typically has high purity and a particle size of $0.02\text{-}2\mu\text{m}$. Both PCC and GCC are used in similar markets but due to its ready availability and cheap production GCC is the most widely used one. [9] However, since PCC is a synthetic product, its physical properties can be controlled during manufacturing by creating PCC of different morphology. As a result, it gives PCC outstanding performance in many applications where GCC does not perform just as well [10]. Furthermore, PCC tends to have a higher brightness, is less abrasive, and has the higher CaCO_3 content compared to GCC [9].

2.1 Production of PCC

The start of commercial production of PCC dates back to 1841, when an English company used residuals from their potassium chlorate production to produce PCC for the first time [10]. At the present time there are several existing methods for PCC production, with the carbonation, Solvay, and lime-soda processes being the most common technologies. All three processes use limestone (CaCO_3) as raw material for lime milk ($\text{Ca}(\text{OH})_2$). The energy intensive process of producing lime milk is based on the calcination of limestone in a lime kiln at temperatures between 900 and 1000°C . In the carbonation process the lime milk solution is bubbled with a CO_2 -containing waste gas which causes the precipitation of CaCO_3 (Eq.1). The carbonation process is the only process where PCC is produced as the primary product and is regarded as the most simple and most cost-efficient production method for PCC. In the Solvay process calcium chloride (CaCl_2) reacts with sodium carbonate to form sodium chloride (NaCl) and CaCO_3 (Eq.2). In the lime-soda process lime milk reacts with sodium carbonate (Na_2CO_3) to form sodium hydroxide (NaOH) and CaCO_3 as a by-product (Eq.3). Certain amounts of impurities (e.g. gypsum) can be found in Solvay- and lime-soda-produced PCC which explains quality differences of PCC produced by different technologies. [2,6,11]

Table 1: Main chemical reactions of the carbonation, Solvay and lime-soda process [6]

Process	Main chemical reaction	
Carbonation	$\text{Ca}(\text{OH})_2 (aq) + \text{CO}_2 (gas) \rightarrow \text{CaCO}_3 (s)$	Eq.(1)
Solvay	$\text{CaCl}_2 (aq) + \text{Na}_2\text{CO}_3 (aq) \rightarrow 2\text{NaCl}(aq) + \text{CaCO}_3 (s)$	Eq.(2)
Lime-soda	$\text{Ca}(\text{OH})_2 (aq) + \text{Na}_2\text{CO}_3 (aq) \rightarrow 2\text{NaOH}(aq) + \text{CaCO}_3 (s)$	Eq.(3)

2.2 Applications of PCC

Calcium carbonate is a very versatile mineral which is commonly used as filler and extender in a wide variety of industries. The global PCC market by application is shown in Figure 1. It can be seen that the pulp and paper industry is the biggest consumer of PCC. Other industrial applications include plastics, paints and coatings, adhesives and sealants, and others. In 2012, Europe was the second largest regional market for calcium carbonate, which corresponds to a share of almost 24% of the total global market [12].

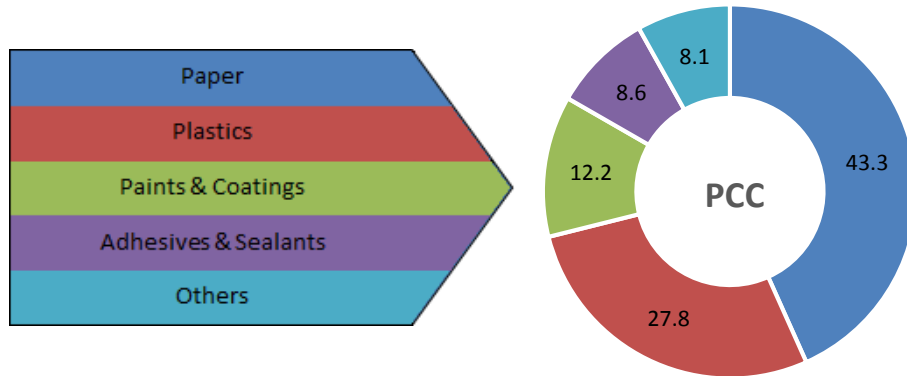


Figure 1: Global end-use market structure for PCC (2013) [13]

Global market projections for calcium carbonate predict to reach 98.7 million tons by 2020, driven by demands from paper and plastic industries [13]. The application of PCC in the pulp & paper and the plastic industry is briefly described in the following paragraphs.

Pulp & Paper industry

In the alkaline papermaking process, PCC is used as filler as well as coating material and is added to the paper in order to improve its optical and physical properties. Different manufacturers have developed a broad range of PCC products with variations in particle-size distribution, crystal shapes and – structures. [14] The variety of crystal morphology and size offers different performance characteristics such as brightness, opacity, and bulk to the paper and can even improve paper machine productivity.

Main properties of PCC that determine the paper quality are purity, crystal morphology, and particle size distribution. [2] The refractive index, brightness, specific surface area, specific gravity, and surface charge are further important parameters influencing the quality of paper. Some of the properties of different commercially available PCC products are compared in Table 2.

Table 2: Properties of commercial PCC products in the pulp & paper industry [2]

Supplier	Application	Morphology	Purity (% CaCO ₃)	Median size d ₅₀ (µm)
SMI	Filler	Scalenohedral calcite	98	1.3-2.2
SMI	Coating	Prismatic calcite	n/a	0.6-2.2
SMI	Coating	Aragonite	n/a	0.4-0.6
Omya	Filler	Scalenohedral calcite	99	1.8
Schaefer Kalk	Multiple appl.	Scalenohedral calcite	99	1-3

The purity of PCC is a very critical parameter since it has a great effect on the brightness of the paper. [2] Mineral impurities such as manganese and iron can cause the PCC to discolour and should therefore be avoided or removed beforehand. Commercial PCC pigments usually have a purity of at least 97%.

Plastic industry

Calcium carbonate is used as an inorganic filler material for the production of polyvinyl chloride, polypropylene, and polyethylene. [15] Calcium carbonate not only functions as an additive to improve the physical performance of the plastic, but also as an auxiliary material for processing to improve the formability of the final products. Another advantage is the lower price compared to other mineral fillers. When used in plastics the PCC particle size combined with the substitution ratio play an important role. Generally, the smaller the PCC particle size, the higher the improvement of physical properties such as impact strength and yield strength are. This is valid for substitution ratios up to 10-15%, above which the strength decreases.

Also nano-PCC has been used in the plastic industry as highly effective impact modifier and filler material. [16] Nano-PCC has an average particle diameter of less than 100 nanometres and allows for high filler loading due to its narrow particle size distribution.

2.3 Morphology

As explained already earlier, PCC is a synthetic product and its physical properties can be controlled during manufacturing. Process parameters such as temperature, pH, the presence of additives, and others, have strong influence on the precipitation process and define the morphology of the precipitate. [17] Generally, calcium carbonate can crystallise into three different polymorphs namely calcite, aragonite and vaterite (see also Figure 2). Despite their different structures they are all chemically identical crystalline forms of calcium carbonate. However, only calcite and aragonite crystal shapes are used commercially.

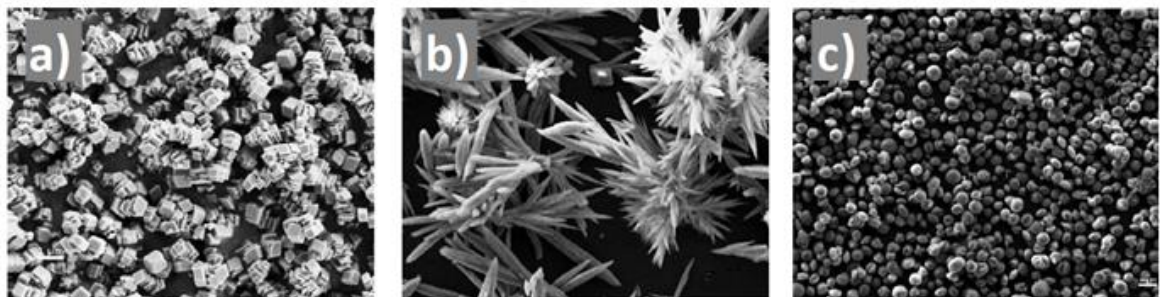


Figure 2: Scanning Electron Microscope pictures of a) rhombohedral calcite, b) aragonite and c) vaterite produced with the X2PCC process. [17]

Calcite is the most stable form, aragonite only forms at higher temperatures ($>50^{\circ}\text{C}$), and vaterite is of metastable nature and usually transforms either to calcite or aragonite. Crystal morphology and particle size are generally influenced by supersaturation [18,19]. Jung et al. [19] pointed out that rather excess species of the reactants than supersaturation are responsible for changes in morphology. In the study by Han et al. [20] additionally to initial concentrations of reactants, flow rate and temperature had an influence on the morphology. The effects of temperature on morphology was also mentioned in several studies [2,18,21–25].

Calcium carbonate can appear in three different hydrated forms, namely as monohydro calcite, hexahydro calcite, and as amorphous calcium carbonate. [26] At low temperatures the crystallization process usually involves the transformation of the unstable amorphous calcium carbonate to calcite via vaterite. At elevated temperatures amorphous calcium carbonate transforms to aragonite via vaterite.

Calcite

The fact that calcite is the most stable form under standard conditions, makes it the most important polymorph when used in different industries. [21] Beside its rhombohedral form, calcite also exists as scalenohedral (star-shaped particles) and prismatic form. Scalenohedral calcite is mainly used as material in paper making and for paints, and rhombohedral calcite in plastics and sealants industries due to its high specific surface area. It has been shown that the particle morphology is dependent on growth rates on crystal faces. [18,27] While a low Ca^{2+}/CO_3^{2-} ratio in precipitation favours the growth process of rhombohedral faces, an increase in the Ca^{2+}/CO_3^{2-} ratio enhances the growth of scalenohedral faces. In other words, under conditions with Ca^{2+} in excess the morphology is scalenohedral.

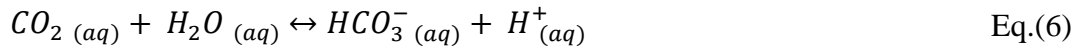
Aragonite

At standard conditions the needle-like aragonite is thermodynamically unstable and tends to alter into calcite. [2] It is used in applications that require high surface area, such as e.g. for paper coatings. As filler material aragonite is also used to improve mechanical properties of polymer materials and paper due to the crystals' high aspect ratios. [28] Moreover, aragonite is denser than calcite and known as a good biomedical material. Many studies [2,18,21–25] have shown that higher temperatures enhance the formation of aragonite.

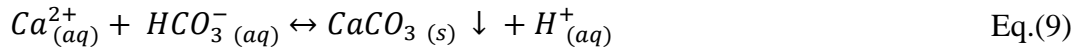
3 Principles of PCC Precipitation

The multistep process of calcium carbonation in a calcium rich solution consists of the absorption of CO₂ on the surface of the aqueous solution, the dissolution of CO₂ in water, and the principal chemical reactions of calcium with carbonate and bicarbonate. The main reactions involved in the precipitation of calcium carbonate are presented in the equations below (Eq. 4-10) [2,29,30].

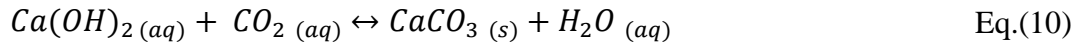
Reaction of carbon dioxide:



Precipitation of calcium:



When CO₂ is excessive:



In general, precipitation can be described as the formation process of a suspension of solid particles as a result of a chemical reaction or physical change [31]. The main steps of precipitation are nucleation and crystal growth. [32] Furthermore, aging, ripening, and agglomeration can occur during the precipitation process.

The main driving force for both nucleation and crystal growth is the supersaturation, which can be defined as the difference in chemical potential of a molecule in solution and a molecule in the bulk of the crystal phase [33].

The initial phase of precipitation is the formation of a nucleus. [32] Nucleation is described as an energy-consuming process that involves the formation of an organized structure from ions or particles in the solution. Depending on whether foreign particles or crystals are present in the solution, the nucleation process can be homogeneous (no foreign particles present) or heterogeneous (presence of foreign particles). In both, heterogeneous and homogeneous nucleation, a certain activation energy barrier has to be overcome so that a nuclei can be formed. If foreign particles are present in the solution, the activation energy barrier is usually reduced, meaning that a lower degree of supersaturation is required compared to homogeneous nucleation. In other words, nucleation occurs much more readily (at a lower supersaturation) if crystals are already present in the solution. Commonly, so called seed crystals are used to not only trigger or enhance crystallization but also to influence and control the crystal size distribution of the final product.

Once the nucleus has outreached its critical size, it is considered to be stable in the bulk of the fluid and from that point onwards it is growing into a crystal of visible size. [34] Whether an unstable nucleus dissolves or a stable one grows, both behaviours aim to minimize the free energy of the system. Mechanisms of crystal growth have been widely studied and many theories, such as surface energy theories or adsorption layer theories have been developed.

If the nucleation step dominates over crystal growth, naturally particles with a small average particle size can be expected. It is also believed that higher levels of supersaturation enhance the nucleation process and therefore result in smaller particles [35].

Aging is defined as the change in crystal structure over time. [32] Sometimes the initially formed crystal structure is not the most stable one, which might lead to its transformation into a more stable crystal structure. The increase in crystal size due to dissolution of small crystals and their re-deposition on the surface of larger crystals is called ripening [34]. The driving force behind this process is the difference in solubility between small and large particles.

It shall be mentioned that supersaturation is not the only factor affecting the precipitation process. Temperature, solution pH, and ionic strength are other important factors that need to be considered when analysing precipitation reaction chemistries. [35] An increase in temperature for example, usually increases the solubility of reactants which furthermore favours the crystalline deposition as previously described. For the efficient collection of the precipitation product the solubility product needs to be as low as possible, meaning that the product should be insoluble.

3.1 Mass Transfer between Gas and Liquid Phase

When gas is absorbed in a liquid, gas molecules are being transferred from the gas side across the gas-liquid interface to the bulk of the liquid phase. [36] The solubility of the gas as well as the mass transfer performance are the determining steps for the final concentration of the solute in the bulk of the liquid.

A common way to describe the solubility of a gas in water is by the Henry's law constant k_H . The constant is usually defined as the ratio of the concentration of a species in aqueous phase to its partial pressure in the gas phase. Findlay and Shen [37] found that the solubility of CO_2 in an ammonium chloride solution is less than in water and decreasing with increasing concentration of the solution. In their study, pressure changes (in a range of 1 to approximately 2 bar) had no effect on the solubility. Experiments by Rumpf et al. [38] conducted over a temperature range of 40°C to 160°C and pressures up to 100 bar, show that the solubility of CO_2 in aqueous ammonium chloride increases with increasing pressure, but decreases with increasing temperature [39].

To describe the mass transfer at the interfacial area a microscopic approach which considers concentration differences between the gas- and liquid phase is necessary. Several theories of mass transfer, such as Whitman's film theory, Higbie's penetration theory, and Danckwerts surface renewable theory have been developed and are used to describe transfer phenomena [40].

3.1.1 Two-film Model

The two-film model describes mass transfer and the evolution of concentration gradients in two stagnant films on each side of the interface. Generally, the two-film theory assumes equilibrium at the gas liquid interface, thus mass transfer encounters resistance from the liquid film as well as from the gas film.

Regarding the precipitation process of calcium carbonate, the gas phase is composed of pure CO₂ and the liquid bulk of an aqueous solution of ammonium chloride. In order to describe the mass transfer in such a system by applying the two-film theory, the following assumptions have been made:

- 1) Since CO₂ is sparingly soluble in NH₄Cl [2] the resistance from the gas side towards mass transfer can be neglected, which means that the main driving force comes from the liquid film [36,41,42].
- 2) Furthermore, concentration in the liquid bulk is assumed to be uniform due to turbulence/agitation.
- 3) The film is considered to be stagnant and always in a quasi-steady state, which means that it absorbs the gas by steady state molecular diffusion [41].

Keeping these assumptions in mind, the mass transfer process can be illustrated as follows:

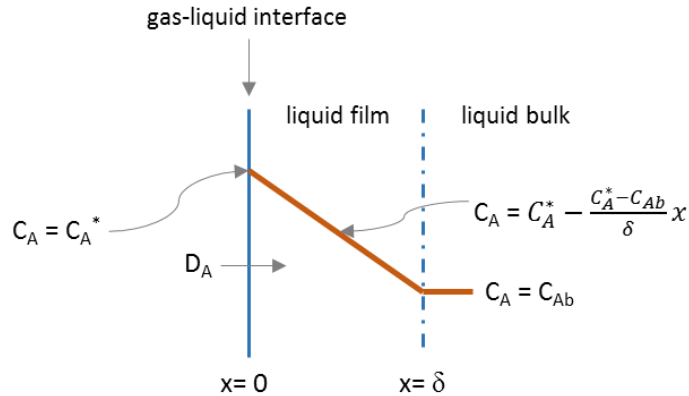


Figure 3: Mass transfer of solute A across the gas-liquid interface

with δ being the film thickness and x the dimensionless distance from the gas-liquid interface towards the liquid bulk. As it can be seen from Figure 3, the concentration of solute A at the gas-liquid interface (C_A) is equal to the concentration at equilibrium with partial pressure of the gas side (C_A^*) and C_{Ab} is the concentration of solute A in the bulk of the liquid. The continuity equation for A can be written as:

$$D_A \frac{d^2 C_A}{dx^2} = 0 \quad \text{Eq.(11)}$$

where D_A is the diffusivity of A. From that, the absorption flux for solute A can be written as:

$$N_A = \frac{D_A}{\delta} \cdot (C_A^* - C_{Ab}) \quad \text{Eq.(12)}$$

which is equal to the concentration difference times the mass transfer coefficient:

$$N_A = k_L \cdot (C_A^* - C_{Ab}) \quad \text{Eq.(13)}$$

This means that according to the film-theory, the mass transfer coefficient (k_L) varies in direct proportion to the diffusivity of A in the liquid. However, it should be noted that the film thickness δ is unknown and that the rate of mass transfer is therefore unpredictable by the two-film theory. Experiments also indicate that the mass transfer coefficient is less than proportional to the diffusivity of A, which is why the theories of Higbie and Danckwerts are often preferred. Their theories predict that k_L is proportional to the square root of the diffusivity of A, which is more precise than Whitman's prediction [41].

3.1.2 Effect of Chemical Reactions on the Mass Transfer

Neither the two-film theory, nor the theories by Higbie and Danckwerts are able to predict the rate of mass transfer; however, they can be used to predict the effect of chemical reactions on the mass transfer. [41] In order to predict the effect of the chemical reaction the film theory shall be applied and the following assumptions shall be made:

- 1.) Solvent A is being transferred from the gas phase to the liquid phase; on the liquid side A reacts with the liquid element B.
- 2.) Both A and B are of first order.
- 3.) B is assumed to be non-volatile, which means that it can't reach the gas phase by vaporization.
- 4.) The resistance from the gas phase can be neglected.
- 5.) There is no accumulation of elements in the interface, which means that the reaction occurs in a steady state.

Generally it can be said that the mass transfer process is being accelerated by the occurrence of a chemical reaction. Therefore, the actual absorption rate can be defined as the physical absorption rate multiplied by the mass enhancement factor E, as given in Eq.14.

$$N_A = E k_L (C_A^* - C_{Ab}) \quad \text{Eq.(14)}$$

The enhancement factor can be written as:

$$E = \frac{\sqrt{M}}{\tanh \sqrt{M}} = \frac{Ha}{\tanh Ha} \quad \text{Eq.(15)}$$

where M is the Diffusion-reaction parameter, which compares the characteristic time for diffusion to the characteristic time for reaction. M can also be expressed as the Hatta number (Ha), which is a very common dimensionless parameter to describe how mass transfer is affected by a chemical reaction and which is simply the square root of M.

Considering the occurrence of a chemical reaction, the continuity equation for A can be rewritten as follows:

$$D_A \frac{d^2 C_A}{dx^2} = k C_A C_B \quad \text{Eq.(16)}$$

where D_A is the diffusion of A in the liquid, C_A is the concentration of A, C_B is the concentration of B, and k is the reaction rate. When comparing Eq. 16 with Eq. 11, it can be seen that Eq. 16 contains an additional reaction rate term on the right hand side of the equation. The equation for B can be written in a similar manner:

$$D_B \frac{d^2 C_B}{dx^2} = b k C_A C_B \quad \text{Eq.(17)}$$

where b is the stoichiometric coefficient of B. In order to obtain comparable values, it has been found useful to treat these equations (Eq.16 and 17) in a dimensionless form by defining dimensionless variables α , β , ζ as:

$$\alpha = \frac{C_A}{C_A^*} \quad \beta = \frac{C_B}{C_{Bb}} \quad \zeta = \frac{x}{\delta}$$

The dimensionless equations for the diffusion of A and B can therefore be rewritten as:

$$\frac{d^2 \alpha}{d\zeta^2} = \left(\delta^2 \frac{k C_{Bb}}{D_A} \right) \alpha \beta \quad \text{Eq.(18)}$$

$$\frac{d^2 \beta}{d\zeta^2} = \left(\delta^2 \frac{k C_{Bb}}{D_A} \right) \left(\frac{b D_A C_A^*}{C_{Bb}} \right) \alpha \beta \quad \text{Eq.(19)}$$

Originating from these equations, it is now possible to define the already mentioned Diffusion-reaction parameter M and the relative abundance parameter q :

$$M = \frac{\delta^2}{D_A} k C_{Bb} \quad \text{Eq.(20)}$$

$$q = \frac{D_B C_{Bb}}{b D_A C_A^*} \quad \text{Eq.(21)}$$

The relative abundance compares the relative rate of supply of B/A to the relative requirement of B/A. For q it can be said that usually $q \gg 1$ since the concentration of A on the liquid side at equilibrium (C_A^*) is much smaller than the concentration of B in the bulk of the liquid (C_{Bb}).

Both M and Ha can be used to determine whether the process involves a fast or slow reaction and whether the chemical reaction occurs in the film or in the bulk of the liquid. For example, if M has a large value, the time for diffusion is larger than the reaction time, which means that the reaction is much faster than the diffusion process. Depending on the value of M/Ha and E , reactions can be classified into slow-, fast- and instantaneous reaction regimes (see also Table 3). It should be mentioned that depending on the source in literature, the Hatta value might be slightly different for different regimes. While Van Elk et al. [43] consider reactions with $Ha > 2$ as fast reactions, Roizard and Wild [42] consider reactions with $Ha > 3$ as fast reactions. Trambouze and Euzen [40] consider reactions with a Hatta value between 0.3 and 5 as moderate, and those with a Hatta value greater than 5 as fast reactions. It was explained by NPTEL [44] that at $Ha = 3$ already a bit more than 90% of the gas are absorbed in the liquid film.

Table 3: Possible regimes for mass transfer accompanied by chemical reaction [40,44]

Slow reaction regime	Fast reaction regime	Instantaneous reaction regime
$M \ll 1, M \ll q$ $Ha < 0.3$ $E = 1$ Reaction in liquid bulk	$M > 1$ $Ha > 3$ $E = Ha$ Reaction in liquid film	$M \gg 1$ $Ha > 3$ $E = 1 + q$ Reaction solely in liquid film

3.1.2.1 Slow Reaction Regime

In cases where M is small and $M \ll q$, and considering that the concentration profile of B is constant throughout the film ($\beta=1$), the reaction of A becomes independent of β . These reactions are so called pseudo-first-order reactions.

In the case where $M \ll q$ and $M \ll 1$ (or $Ha < 0.3$), the reaction equation of A becomes the same equation as the physical mass transfer equation (Eq. 11). This also means that the reaction occurs outside the film in the liquid bulk, where the concentration of A is affected by the chemical reaction. It is possible to distinguish between two sub-regimes within the slow reaction regime, namely the kinetic sub-regime and the diffusional sub-regime (see also Figure 4). The only difference between these sub-regimes is their value of P . The parameter P compares the amount of A which could react in the liquid bulk to the maximum flux of A which could be transferred through the gas-liquid interface in the absence of a chemical reaction (see also Eq. 22). [42,45]

$$P = \frac{kC_{Bb}}{k_L \hat{a}} \quad \text{Eq.(22)}$$

where \hat{a} is the interfacial area per unit volume of liquid.

In the kinetic sub-regime the chemical reaction in the bulk is slow enough and the mass transfer rate large enough, so that the concentration profile of A is flat (see Figure 4 case b). The concentration of A in the bulk (C_{Ab}) is close to its saturation concentration C_A^* . In the diffusional sub-regime, the reaction is so fast, that the concentration of A in the bulk reaches zero (see Figure 4 case c).

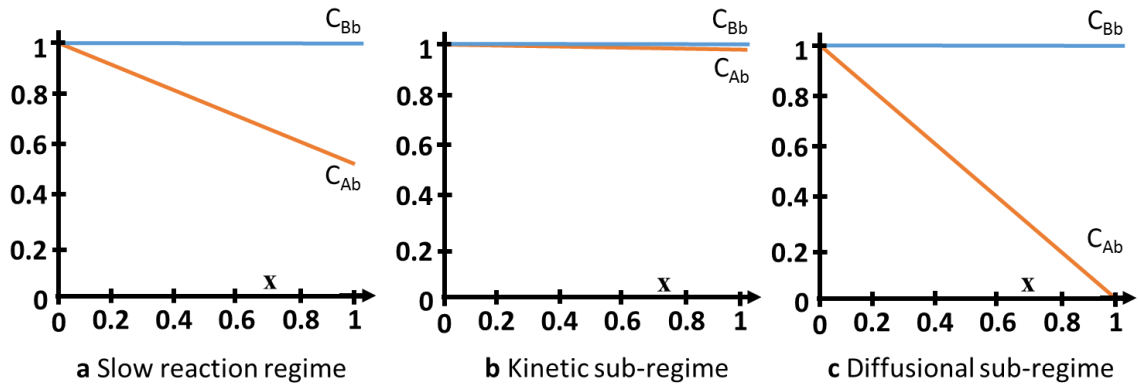


Figure 4: Concentration profiles of A and B in the liquid bulk under the slow reaction regime (adapted from [40])

3.1.2.2 Fast Reaction Regime

With an increasing Hatta number the kinetic regime progresses from a slow to a fast reaction regime. The concentration profile of B can no longer be assumed to be uniform (M is no longer much smaller than q) and the second order nature of the reaction has to be considered.

For fast reactions with $Ha > 3$ the enhancement factor E is approximate to Ha and the reaction process primarily occurs in the gas-liquid interface, which means that absorption kinetics are mainly controlled by mass transfer. The higher the Hatta value becomes, more and more gas that has been absorbed at the gas liquid interface is being consumed by the chemical reaction in the film. Once the Hatta number reaches a high enough value so that the gradient of α becomes zero, the reaction is considered as a fast reaction. This also means that the entire flux of A entering the film is being consumed in the film by the chemical reaction, and no A is being transferred into the liquid bulk ($C_{Ab} \approx 0$).

3.1.2.3 Instantaneous Reaction Regime

The case of an instantaneous reaction can be explained as a process where the reaction zone of A and B within the film becomes thinner and thinner with increasing value of Ha . When the reaction reaches the point where there is no region within the film where A and B can coexist, both the concentrations of A and B become linear with respect to x (see Figure 5).

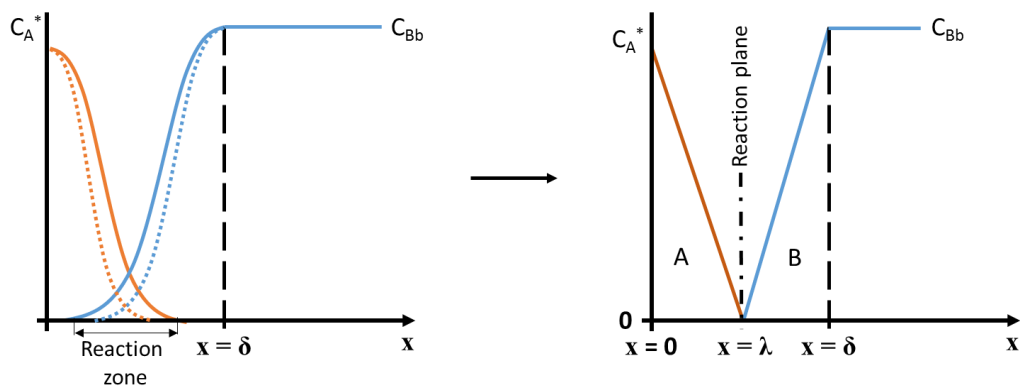


Figure 5: Transition from fast reaction regime to instantaneous reaction regime

From Figure 5 it can be seen that, when $x=0$ the concentration of A is $C_A = C_A^*$ and the concentration of $C_B=0$. At the point where $x=\lambda$ the concentration of A is $C_A=0$, while at $x=\delta$ the concentration of B is $C_B=C_{Bb}$.

The (infinite) enhancement factor for an instantaneous reaction can be written as follows:

$$E_\infty = \frac{D_A C_A^* / \lambda}{D_A C_A^* / \delta} = \frac{\delta}{\lambda} = 1 + q \quad \text{Eq.(23)}$$

which is the mass transfer rate of A with reaction over the mass transfer rate of A without reaction.

3.1.3 Internal Circulation

In the past, the effect of internal circulation on the mass transport has been subject to many studies [46–50] and has been found to be an important factor for the mass transfer of a moving liquid droplet. Internal circulation (depicted in Figure 6) occurs due to shear stress on the surface of the droplet, which in turn creates vortices inside the drop. Shear stress is induced by velocity gradients inside the boundary layer due to the relative motion between the droplet and the surrounding fluid.

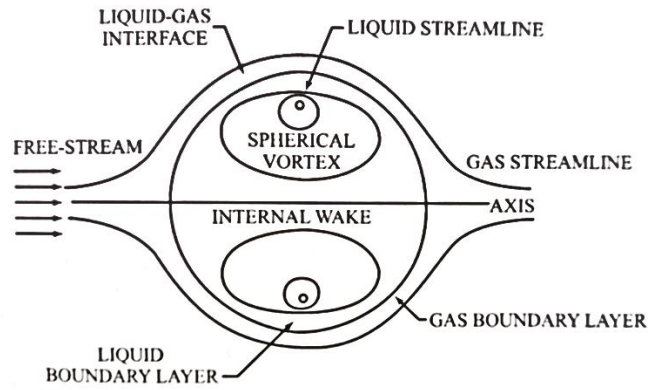


Figure 6: Droplet with relative gas-droplet motion and internal circulation [51]

With increasing Reynolds number (Re) the effect of internal circulation on the mass transport becomes noticeable and the interfacial mass transfer is being enhanced. For droplets with low Reynolds number, internal circulation becomes insignificant and the mass transfer in the droplet occurs primarily by molecular diffusion [46,47,52]. Chen et al. [46] for example studied the absorption of CO_2 by atmospheric aerosol droplets and compared the mass transfer process of droplets with $Re=0.1$, $Re=1$, and $Re=10$. The results of the study show that the mass transport in droplets with $Re=0.1$ was dominated by radial diffusion; for droplets with $Re=10$ the internal vortices played an important role in mass transport.

3.1.4 Mass Transfer of the CO_2 - $Ca(OH)_2$ System

The Hatta number for the reaction of CO_2 with $Ca(OH)_2$ is according to a study by Schnebelen et al. [53] 2.9, which means that the reaction will predominantly occur in the liquid phase film (mass transfer controlled kinetics). Because of that, the supersaturation as well as the nucleation rate in the film will be very high. CO_2 in the liquid interface will be

consumed very fast and only very little amount will be present in the bulk of the liquid. Furthermore, due to the small volume of the liquid film, compared to the suspension volume, PCC is quickly diluted in the bulk, where the PCC crystal starts to grow. The liquid film phase can therefore be considered as the nucleation zone, while the bulk represents the growth zone of the crystal.

It can be assumed that CO_2 is consumed totally during the precipitation reaction and since the reaction is so fast, it can be said that the degree of supersaturation of CaCO_3 is depending on the absorption rate of CO_2 . [54] The mass transfer of CO_2 from the gas phase to the liquid phase is therefore the controlling mechanism of the absorption-reaction process.

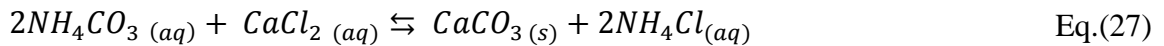
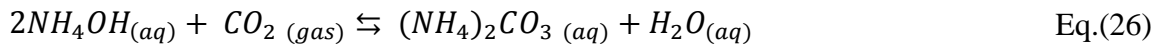
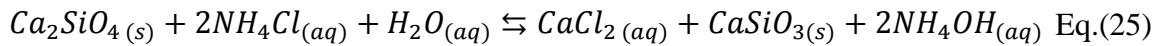
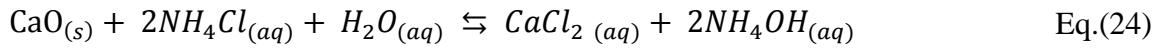
Geankopolis [55] suggests that for systems in which the mass transfer rate is controlled by the liquid film resistance, overall mass transfer can be increased by increasing turbulence in the liquid phase. A more recent study by Han et al. [56] shows that the average liquid phase mass transfer coefficient can be increased by increasing velocity of the droplet.

Bang et al. [57] studied the effects of CO_2 bubble size on the size of CaCO_3 particles using two different calcium sources. For their tests a microbubble generator as well as an air diffuser were used to generate PCC. The study shows that CaCO_3 particles produced via the microbubble generator were smaller and had a larger specific surface area than the particles that were produced with the air diffuser, disregarding the source of calcium.

4 X2PCC Process

The X2PCC process is based on an indirect carbonation process, where calcium is first extracted from steel slag using an aqueous ammonium salt solution, which is then carbonated in a second reactor vessel. Bubbling CO₂ into the Ca-rich solution causes the precipitation of CaCO₃ in the carbonation reactor.

The main chemical reactions of the X2PCC process are presented in Eq.24-27:



where Eq.24 and Eq.25 are the main reactions of the extraction stage, and Eq.26 and Eq.27 the main reactions of the carbonation stage.

The main advantage of the X2PCC process over conventional technologies, such as the carbonation process, is the possibility to convert CO₂ into a marketable product by using slag, an industrial waste material. The technology allows to save virgin material resources, such as limestone, and reduce CO₂ emissions at the same time. A very important feature of the process concept is the possibility to operate the system at ambient temperature and pressure, which results in a lower energy demand [58]. Another important characteristic of the X2PCC process is the reutilization of ammonium salt (NH₄Cl). As it can be seen from the reactions above as well as from the schematic in Figure 7, the ammonium salt which is consumed in the extraction stage (Eq.24), is regenerated in the carbonation stage (Eq.27), allowing it to be recycled to the process.

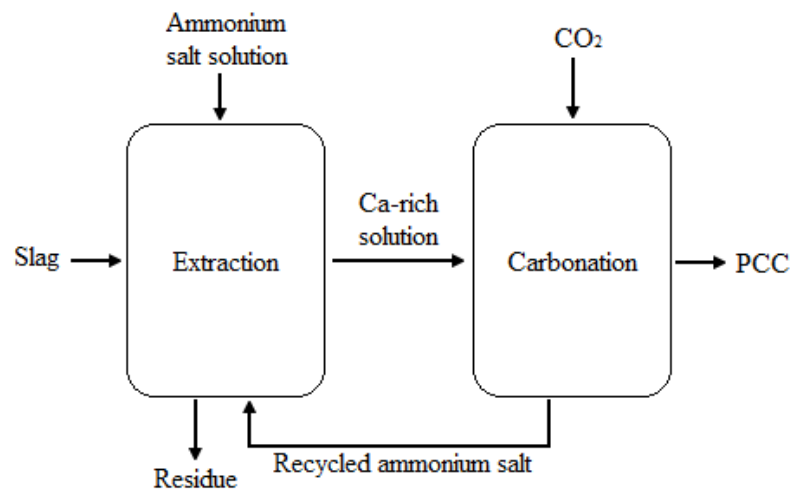


Figure 7: Simplified schematic of the X2PCC process

The slag which is used in the X2PCC process is a non-metallic by-product from the steelmaking process and contains calcium, magnesium, and aluminium silicates in different combinations. [3] The potential of steel slag for the production of PCC has already been illustrated by several authors in the past [2,6,11,59]. In Europe steel slag is mainly used in road construction, but due to its higher amount of free lime (CaO), its usage as construction material is more restricted than that of other slag types. [2] This is why usually more than 10% of produced steel slag end up in landfills, which in turn is where readily available steel slag for the production of PCC can be found.

In the first step of the X2PCC process, calcium is selectively extracted from the slag using an aqueous solution of ammonium chloride. The extraction process at room temperature takes typically 60 minutes after which the mixture is filtrated in a filtration unit to separate the Ca-rich solution from the residual slag. The Ca-rich solution is then pumped to the carbonation reactor, where CO₂ is bubbled into the solution via a gas sparger. The gas sparger has 400 holes and each hole as a diameter of 0.5 mm. Based on the gas sparger orifice radius (r_o) the CO₂ bubble size (bubble radius r_{bub}) can be estimated as shown in Eq. 28:

$$r_{bub} = \left(\frac{3}{2} \frac{r_o \sigma}{\Delta \rho g} \right)^{1/3} \quad \text{Eq.(28)}$$

where σ is the surface tension, $\Delta \rho$ the density difference between the liquid and the bubble, and g the gravitational constant. The CO₂ bubble radius of the X2PCC process was calculated to be 1.38 mm, assuming a surface tension of 72 mN/m (surface tension of water in contact with air at 298K and 1 bar) and considering the density difference between the Ca-rich solution ($\rho = 1030 \text{ kg/m}^3$ at 25°C [25]) and CO₂ ($\rho = 1.815 \text{ kg/m}^3$ at 25°C). After the completed carbonation, the solution is filtered in order to collect the PCC. Roughly, for each kilogram of slag around half a kilogram of PCC can be produced.

The production of PCC with the X2PCC pilot plant has been successfully demonstrated, as rhombohedral calcite, aragonite, aragonite/calcite mixtures, as well as small amounts of vaterite were produced in the past. Since the commercial viability of the X2PCC process is dependent on the quality of the produced PCC, accurate control over the precipitation conditions is of extreme importance. The final quality is dependent on many different parameters, which affect the extraction and/or the carbonation steps. Such parameters include solvent concentration, particle size, solid-to-liquid ratio, temperature, pH, supersaturation, residence time, bubble size and many others. The main challenges of this technology are currently in ensuring the desired particle size and crystal shape. In order to collect as much as possible of the produced PCC from the reactor, efficient reactor washing plays an important role as well.

4.1 Main Findings from Previous Experimental Studies

With the goal to produce high-quality PCC from steelmaking slag, extraction and carbonation mechanisms have been studied very intensively and a lot of experimental work has been done over the past few years. Main findings from these studies are presented in this section and shall give a better understanding of the overall process and its determining parameters. An extensive literature review on factors affecting the extraction of calcium and the precipitation of PCC is also presented in the work of Zappa [2].

4.1.1 Parameters Affecting Calcium Extraction Efficiency

Mattila et al. [30] studied the effects of different parameters on the extraction process by both using a chemical kinetics model and conducting experimental tests. Main factors affecting the speed of calcium extraction were found to be size and age of slag particles, and the solid-to-liquid ratio (SLR). Also the solvent concentration of the solution was found to be an important parameter, whereas the temperature of the solution had only negligible influence on the extraction efficiency [30,60].

Eloneva et al. [61] tested different solvents for dissolving calcium from slag and concluded that ammonium salt solutions seem to be the most promising solvents. To avoid the dissolution of other impurities from the slag, 1M was considered to be the optimum solvent concentration [62].

Eloneva et al. [63] as well as Said et al. [6] studied the effect of slag's grain size on the calcium extraction efficiency and found that the smaller the grain size, the higher the extraction efficiency. They also found that extraction efficiency decreases with increasing SLR. The same correlation was acknowledged by Zappa [2], however, the higher SLR did not decrease extraction efficiency as much as expected from the work by Said et al. [6]. Further experiments were recently conducted by Sundermann [25] trying to increase the calcium concentration by changing the SLR. So far, a SLR of 0.1 was found to be the most effective ratio for calcium extraction and also the current tests could not disprove previous findings.

Other experiments used ultrasound technology to increase calcium extraction efficiency. [62] The results showed that sonication significantly improves the extraction efficiency and that the dissolution of calcium from small as well as large particles is higher compared to mechanical agitation (31 and 20 percentage points respectively).

Later, another research by Said et al. [1] showed that extraction efficiency can also be improved by using a two-stage calcium extraction process. Results from their solvent recyclability tests also revealed that the solvent solution can be recycled up to 10 times before the extraction efficiency drops significantly.

4.1.2 Parameters Affecting Precipitation

Sundermann [25] investigated the morphology of PCC as a function of the initial calcium concentration. It was found that at low and high initial calcium concentrations (≤ 12 g/L and ≥ 23 g/L) calcite is the predominant form, while aragonite was formed in between. For the effect of initial supersaturation on the morphology, Sundermann observed that supersaturation levels below 4.5 favour the formation of aragonite. The main crystal form found at higher supersaturations was calcite, while vaterite was only found to a very small extent at the highest supersaturations.

During the carbonation process OH⁻ ions are being consumed, which causes the pH to drop. In the experiments conducted by Sundermann [25], it was observed that stopping the carbonation at a low end pH (<8.5) mainly causes the formation of calcite, while higher end pH (>8.5) favours the formation of aragonite. The test time for experiments with low end pH usually took more than an hour. Also the start pH seemed to have an influence on the

morphology, as a pH at a range between 9.5 and 10.3 seems to favour the formation of aragonite.

As mentioned in Chapter 2.3, high carbonation temperatures (usually above 55°C [1]) favour the formation of aragonite particles. In the X2PCC process high carbonation temperatures however result in the evaporation of ammonia (NH₃) from the ammonium chloride solution. Said et al. [1] found that the NH₃ content in the flue gas is more than 2 vol.% at 60°C, while it is only 0.11 vol.% at 45°C. Sundermann [25] investigated the dependency of morphology on temperature and found that calcite was the main form at 35°C, while large amounts of aragonite were formed above 45°C. A further increase in temperature from 45°C to 54.5°C showed however only little changes in morphology. Based on her results, Sundermann concluded that temperature, pH and test time are the most important factors influencing the morphology of PCC.

5 Spray Carbonation

Both the conventional X2PCC process as well as the currently studied spray carbonation process deal with a dispersed form of two-phase flow. While the liquid is the continuous phase and the gas the discrete phase for the conventional X2PCC process, it is the opposite for the spray carbonation process. Former also known as bubbly flow and later being a spray type of flow. The disintegration of a liquid into small droplets is generally defined as atomization and the suspension of fine droplets in a gaseous atmosphere is called spray. [64] Applications using discrete droplets make use of the large surface areas of droplets to achieve high reaction rates and to increase heat- and mass-transfer. Droplet properties, such as droplet shape and size, have an important impact on the transport phenomena. The break-up of a liquid jet flowing through a nozzle into the gaseous atmosphere is one possibility to create a spray. A spray tower is a device in which gas-liquid contact between fine droplets and a gas stream is created. Advantages of a spray tower are a low pressure drop in the gas phase (compared to e.g. packed towers), simple mechanical construction, and a wide range of liquid to gas loading ratios. [65] Coalescence of droplets and impingement on the reactor wall however can be responsible for the reduction of interfacial area between the gas and liquid phase which can result in lower mass transfer rates.

5.1 Spray Carbonation Process

A simple schematic of the spray carbonation process considered in this study is presented in Figure 8. At the heart of the process is the spray carbonation reactor, or also called spray tower, where the Ca-rich solution is dispersed into the tower in counter-flow to the gas stream.

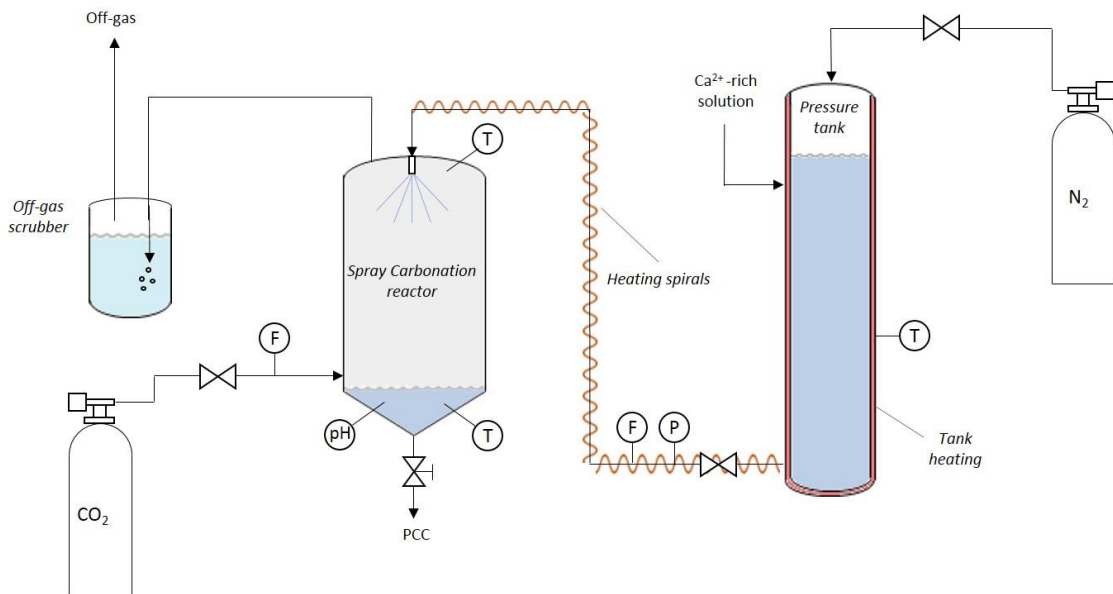


Figure 8: Simple schematic of the spray carbonation process

While CO₂ enters the reactor from the lower bottom, a pressure nozzle at the top of the reactor is used to disperse the solution into the reactor. The energy for atomization is entirely provided by the pressure of the feed liquid, which is pressurized in the pressure tank as shown in Figure 8. Heating spirals and a heating mantle allow heating up the calcium solution in the pressure tank to the desired temperature. Solvent liquid and PCC are collected

at the bottom of the reactor while the off-gas leaves the reactor from the top. An additional off-gas scrubber is used to capture eventual particles, like PCC, from the gas stream. The scrubber is halfway filled with water to avoid particles being released into the atmosphere. Both the top and bottom lid of the spray tower can be removed for cleaning and mounting purposes.

5.1.1 Spray Nozzle

In the conventional X2PCC process CO₂ is bubbled through the calcium rich solution using a gas sparger. Using a spray nozzle allows to create much smaller droplets and therefore a much larger interfacial surface area between the gas and liquid, which is one of the most important criteria when looking at mass transfer [66]. The function of the spray nozzle in the spray carbonation reactor is to convert the Ca-rich solution into droplets and to bring them into contact with the carbon dioxide gas in the spray column. The droplet size produced by a spray nozzle is mainly influenced by the operating pressure of the nozzle, the spray angle, the orifice diameter, and the nozzle's flow capacity. [67] The nozzle design or type itself determines the spray pattern and also affects the final droplet size. Principally, droplet size is decreasing when pressure and temperature are increasing; in contrast, the droplet size increases for fluids with higher viscosities and higher surface tension.

Generally, nozzles with a spray angle of 30° to 60° are recommended for long and narrow chambers [68]. For the experiments with the laboratory-scale test plant oil burner nozzles with different capacities and spray angles were chosen. Oil burner nozzles are available over a wide range of capacities in various spray angles and patterns. The selected nozzles are listed in Table 4.

Table 4: Selected nozzles for experimental work

Manufacturer	Capacity [GPH / L/min]	Spray angle [°]	Nozzle type
Monarch	5.50 / 0.35	60	PLP – semi hollow
Monarch	5.50 / 0.35	30	HV – narrow spray angle
Monarch	0.60 / 0.04	45	R – full cone
DANFOSS	5.50 / 0.35	45	S – full cone
DANFOSS	0.60 / 0.04	45	S – full cone
DANFOSS	1.50 / 0.09	45	S – full cone
DANFOSS	2.50 / 0.16	45	S – full cone

The Monarch 5.50 GPH 60° PLP nozzle has a semi hollow spray pattern, meaning that up to a capacity of around 13 L/h the spray pattern is that of a full cone spray, with increasing capacity however a hollow cone spray pattern evolves. The spray patterns of the chosen nozzles are illustrated in Figure 9.

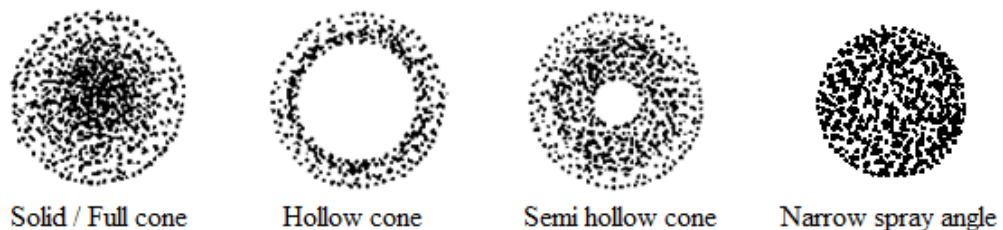


Figure 9: Nozzle spray patterns (Adapted from [69])

The considered nozzles are tested with a test oil similar to No. 2 fuel oil at a nominal pressure of 6.895 bar (100 PSI) [69,70]. The density of the oil is given to be 0.840 kg/L and 1 GPH equals 3.785 L/h. The relationship of nozzle capacity and spraying pressure is defined as following:

$$\frac{Q_2}{Q_1} = \frac{(p_2)^n}{(p_1)^n} \quad \text{Eq.(29)}$$

where Q_1 is the rated flow rate (in L/min) at the rated pressure p_1 (in bar), and Q_2 is the desired flow rate at the desired pressure p_2 . The flow exponent “n” is depending on the specific nozzle type and gives a ratio of pressure to flow. From the following equation

$$\frac{Q_2}{Q_1} = \sqrt{\frac{SG_1}{SG_2}} \quad \text{Eq.(30)}$$

it can also be seen that heavier fluids will have a lower flow rate based on their specific gravity (SG). With the given data the capacity of each nozzle for water and the Ca-rich solution at a pressure of 5 bar has been estimated (see Table 5). For the semi-hollow cone and the narrow spray angle nozzles the exponent was chosen to be 0.50 and for the full cone nozzles 0.46 [71].

Table 5: Estimated nozzle capacities for water and the Ca-rich solution at a spraying pressure of 5 bar

Stated capacity [GPH]	Capacity for H ₂ O at 7 bar [L/min]	Capacity for H ₂ O at 5 bar [L/min]	Capacity for Ca-rich solution at 5 bar [L/min]
0.60	0.035	0.030	0.029
1.50	0.087	0.075	0.074
2.50	0.145	0.125	0.123
5.50 ^{DANFOSS}	0.318	0.274	0.270
5.50 ^{Monarch}	0.318	0.271	0.266

Depending on the capacity of the nozzle, the CO₂ flow rate into the spray tower needs to be adjusted accordingly. Considering the reaction of Ca^{2+} with CO_3^{2-} to form $CaCO_3$ and assuming that the concentration of CO₂ is equal to the concentration of CO_3^{2-} , for each mole of Ca^{2+} one mole of CO₂ is needed for the reaction to proceed under stoichiometric conditions. Given that the calcium concentration of the Ca-rich solution is 20 g/L and knowing the capacity of each nozzle, the required volume flow of CO₂ is the following:

Table 6: Estimated stoichiometric volume flow of CO₂ into the spray tower

Nozzle	Volume flow of CO ₂ [L/min]
Monarch 0.60 GPH 45° R	0.353
DANFOSS 0.60 GPH 45° S	0.353
DANFOSS 1.50 GPH 45° S	0.896
DANFOSS 2.50 GPH 45° S	1.493
DANFOSS 5.50 GPH 45° S	3.283
Monarch 5.50 GPH 60° PLP	3.235
Monarch 5.50 GPH 30° HV	3.235

5.1.1.1 Aerodynamic Properties of the Spray

A droplet falling through a fluid will experience a series of different forces, with gravity and drag being the primary forces (see also Figure 10). Beside the frictional drag which counters the downward gravitational force, virtual mass- and Basset forces as well as pressure and the viscous effect of the surrounding fluid also affect the motion of a droplet.

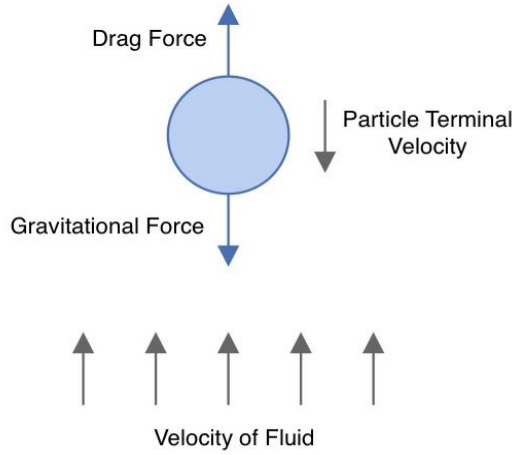


Figure 10: Main forces acting upon falling droplet [72]

The velocity (u_e) of the droplets at the exit of the spray nozzle can be defined as a function of the flow rate and the orifice diameter (d_o). Considering the counter current-flow configuration inside the spray tower, droplets will travel through the tower until they reach their terminal velocity. At terminal velocity a velocity equilibrium between the droplets and the surrounding gas has been reached, meaning that drag force and gravity force are equal. The terminal velocity of a droplet can be defined as follows:

$$u_{td} = \sqrt{\frac{4g d_d(\rho_d - \rho_g)}{3 C_D \rho_g}} \quad \text{Eq.(31)}$$

where g is the gravitational force, C_D is the drag coefficient, and ρ_d and ρ_g are the density of the droplet and the gas phase respectively. The value of the dimensionless drag coefficient depends on object size, object position, flow speed, flow direction, fluid density as well as fluid viscosity and can therefore be described as a function of Re [73]. The Reynolds number based on the relative velocity is given as:

$$Re = \frac{\rho_g d_d (u_d - u_g)}{\mu_g} \quad \text{Eq.(32)}$$

where u_d and u_g are the droplet and gas velocity respectively, and μ_g is the viscosity of the gas. The dependence of the drag coefficient on the Reynolds number is often presented in the form of a curve, the so called ‘‘standard drag curve’’. To approximate this curve many equations have been proposed and a list of these empirical or semi-empirical equations can be found from the work by Clift et al. [73]. Table 7 shows the recommended drag correlations for Reynolds numbers up to 1.2×10^4 .

Table 7: Recommended drag correlations; $w = \log_{10} Re$ [73]

Range	Correlation
$0.01 < Re \leq 20$	$\log_{10} \left[\frac{C_D Re}{24} - 1 \right] = -0.881 + 0.82w - 0.05w^2$
$20 \leq Re \leq 260$	$\log_{10} \left[\frac{C_D Re}{24} - 1 \right] = -0.7133 + 0.6305w$
$260 \leq Re \leq 1500$	$\log_{10} C_D = 1.6435 - 1.1242w + 0.1558w^2$
$1.5 \times 10^3 \leq Re \leq 1.2 \times 10^4$	$\log_{10} C_D = -2.4571 + 2.5558w - 0.9295w^2 + 0.1049w^3$

To ensure that droplets are not entrained with the gas stream and that carry over is minimized, the velocity of the gas relative to the droplet must be smaller than the terminal velocity of the droplet. In typical spray towers with droplet sizes of a few hundred micrometres the time to reach terminal velocity is usually very short. [74] It can therefore be assumed that the droplet falls at a steady terminal velocity through the tower, at least for most of the time.

Based on the information given about the selected nozzles the terminal velocity can be calculated using the equations and correlations mentioned above. Since the nozzles' droplet sizes are initially not known, different values have been assumed. The correlation between terminal velocity and droplet size by taking the example of the Monarch 5.50 GPH 60° PLP nozzle is shown in Table 8. With a capacity of 0.266 L/min and an orifice diameter of 1 mm, the exit velocity was calculated to be 5.64 m/s. The relative velocity between the droplet and the counter flowing gas stream is 6.33 m/s, based on a gas velocity of 0.69 m/s. The terminal velocity for the given example ranges from 0.12 m/s to 1.05 m/s, showing that smaller droplets have a lower terminal velocity.

Table 8: Correlation between terminal velocity and droplet diameter by the example of the Monarch 5.50 GPH 60° PLP nozzle

Droplet diameter [mm]	10.00	50.00	100.00	150.00
Reynolds number	7.81	39.06	78.11	117.17
Drag coefficient	5.06	1.81	1.24	1.00
Terminal velocity [m/s]	0.12	0.45	0.77	1.05

In the design of spray towers it is also common to determine the tower height based on the terminal velocity. From the tower height $H = u_{td} t$, it becomes clear that by decreasing the droplet size and therefore decreasing the terminal velocity the tower height can be reduced. With t being the time needed for the precipitation of calcium carbonate and assuming that the reaction occurs almost instantaneously (in a matter of milliseconds), the distance needed for a droplet to reach terminal velocity is very short.

To optimise mass and chemical transport between droplets and the gas phase it is desirable to reach a stable operational state of counter-current two-phase flow in the spray tower. The interactions between droplets and the gas stream are visualized in Figure 11. It shall be noticed that equations for mass, momentum as well as energy are interdependent. Interactions between droplets and the gas stream greatly affect droplets' trajectories and their residence time in the spray tower. [75] Additionally, interactions between droplets and between droplets and the tower wall can cause coalescence, agglomeration, breakage,

deposition or similar effects. As one would expect, droplet-droplet interactions are originated in regions of high droplet concentration, particularly nearby the spray tower wall and in the close proximity of the spray nozzle. By optimizing parameters such as tower height, spray nozzle type, gas injection position, etc., these effects can be minimized or avoided.

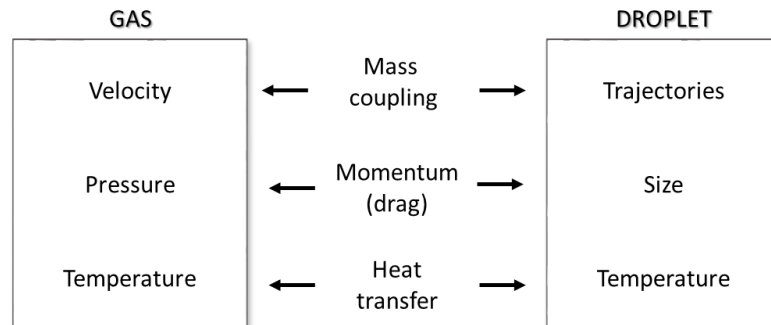


Figure 11: Droplet-gas interactions (Adapted from [76])

6 Experimental Work

The experimental part of this work is divided into two parts. The first part covers the spray analysis which had been performed in order to analyse the spray nozzles and determine their droplet sizes. The second part covers the actual spray carbonation experiments which were carried out with the laboratory-scale test plant.

6.1 Spray Analysis

To analyse the nozzles and to find out their droplet sizes, measurements were recorded using the Malvern particle sizer 2600. The operating principle of the Malvern particle sizer is the measurement of scattering light via a laser beam. A typical experimental configuration is shown in Figure 12. Any particles introduced to the beam of the Helium-Neon laser will scatter the laser light onto the receiver lens, which operates as a Fourier transform lens. The scattered light is then collected by a detector, which creates an electronic output signal proportional to the light energy measured. The scattered light is measured over a range of 31 separate solid angles of collection. Depending on the angle of observation, each particle scatters light with a unique light intensity. The particle's individual energy peak can then be related to its diameter. [77]

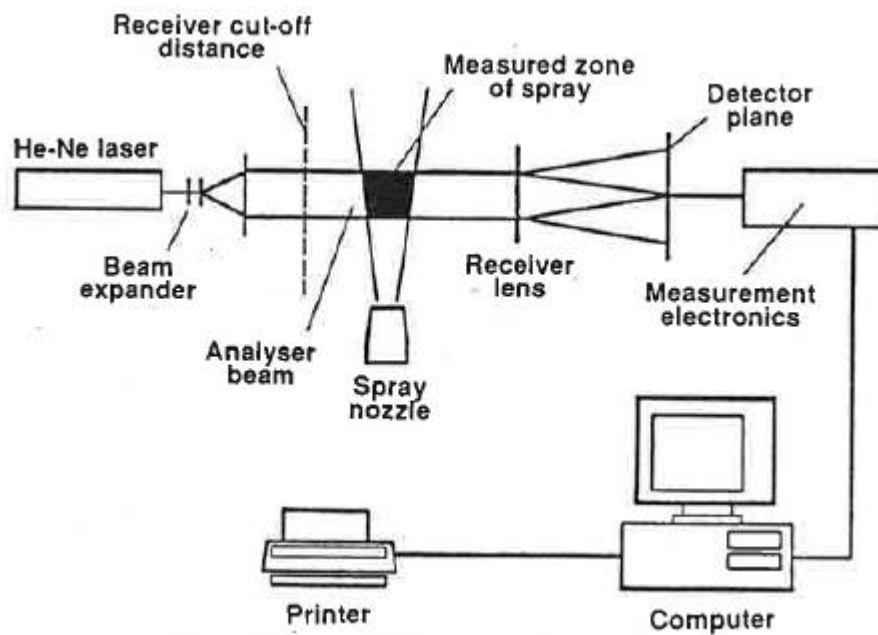


Figure 12: Typical experimental configuration for spraying tests with Malvern particle sizer [77]

6.1.1 Methodology

Before the measurements were started the optical measurement unit was aligned so that the laser beam was focused on the centre detector. After the alignment of the optical unit the background scattering inherent was measured. This measurement is used by the analysis program to subtract background scattering sources from future sample measurements. In order to check whether the laser intensity is still good and the alignment in an acceptable range, the background scattering inherent was measured again after the sample measurements were recorded. For this spray analysis a range lens of 300 mm was chosen. The lens covers a range from 5.8 to 564 μm and the suggested distance of the sample to the lens is less than 400 mm. Only particles that pass through the beam within this cut-off

distance can be measured by the range lens. Each spray nozzle was horizontally positioned, with the laser beam passing through the centre line of the spray cone. To exhaust the spray after it has passed through the laser beam and additionally to avoid any back circulation of the spray, a plastic pipe was placed across from the nozzle in close distance to the laser beam. The Monarch 5.50 GPH 60° nozzle was positioned so, that the nozzle-to-laser beam distance was first 2 cm and then 4 cm. Because of their narrower spray angle, the other nozzles were only tested at a distance of 4 cm from the laser beam. Given their small capacity, the Monarch 0.60 GPH 45° nozzle and the DANFOSS 0.60 GPH 45° nozzle were only tested at higher pressure levels (5 and 4/4.5 bar).

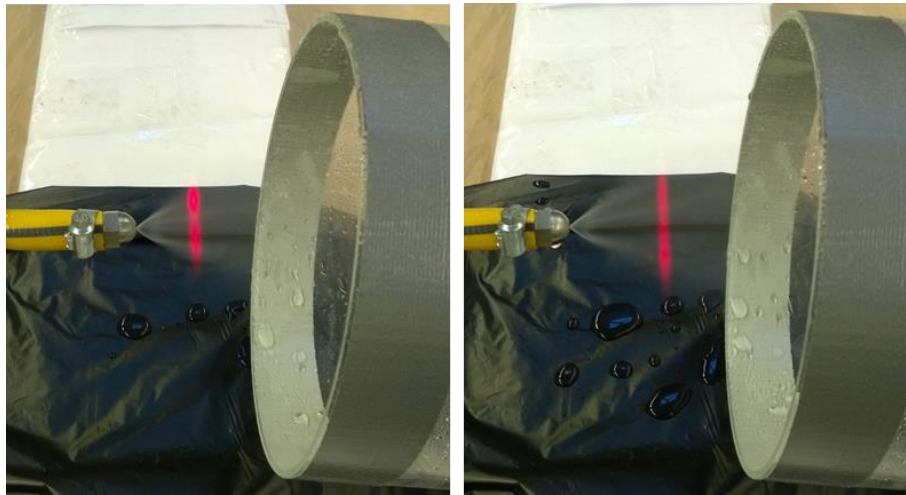


Figure 13: Positioning of the Monarch 5.50 GPH 60° nozzle; left picture: 20 mm nozzle-to-laser beam distance; right picture: 40 mm nozzle-to-laser beam distance

The nozzle itself has been attached to a water hose, which was connected to the water tap in the laboratory. A pressure gauge as well as a shut off valve were used to measure and control the pressure during the measurements. The water temperature was measured with a Fluke 52 K/J thermometer.

For the measurements the liquid-droplet-spray scattering experiment type, based on Fraunhofer diffraction, was chosen. The Fraunhofer diffraction model assumes that particles scatter light like discs of the same diameter. The analysis to obtain a volume distribution from light scattering data is based on the so-called model independent analysis, which is not constrained to be of particular mathematical form since no assumptions about the form of the result are made. The number of sweeps was set to 5000.

6.1.2 Results

In total, a number of 114 measurements were recorded with the Malvern particle sizer. In between, the background scattering was measured and if necessary the optical measurement unit was realigned and the measurements were repeated. In order to be able to compare droplet sizes with PCC particle sizes, the results for droplet sizes are reported on a volume basis. A complete table with all measurement data can be found from Appendix A.

At first, the mean droplet diameter of the Monarch 5.50 GPH 60° nozzle at pressures of 5 bar, 4 bar, 3 bar, 2.6 bar, and 1.8 bar was measured and an average was calculated for each pressure level. Operating the nozzle with a water pressure below 2 bar resulted in an underdeveloped spray cone, which is why only measurement results between 2.6 and 5 bar

are illustrated in Figure 14. From the graph it can be seen that droplet size decreases with increasing pressure. The average volume-based diameter at 5 bar was calculated to be 81.37 μm (at a nozzle-to-laser beam distance of 4 cm) and 102.34 μm (at a nozzle-to-laser beam distance of 2 cm). All droplets measured with the nozzle being 2 cm from the laser beam had a higher diameter compared to the ones where the distance from the nozzle to the laser beam was 4 cm. This is probably due to the reason that closer to the nozzle orifice, large droplets have not yet been broken down to smaller ones.

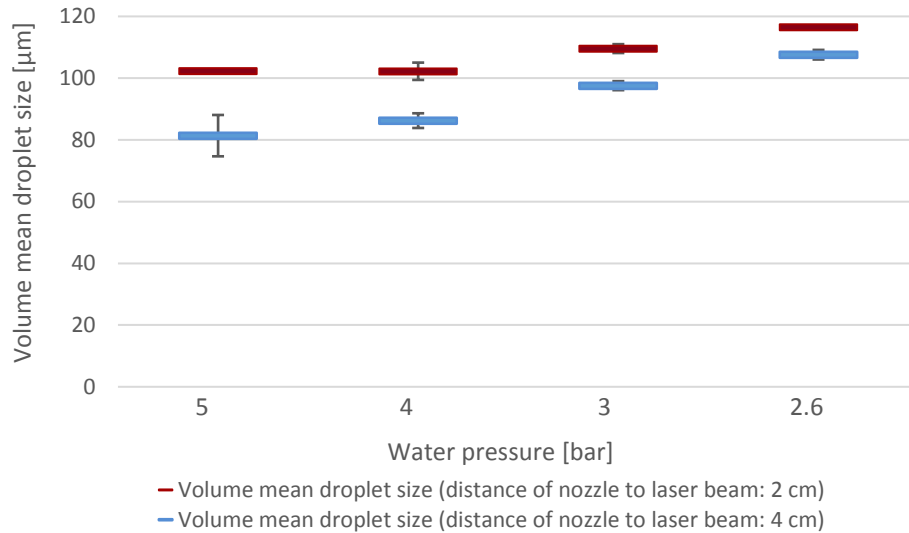


Figure 14: Mean diameter and standard deviation of spray droplets of Monarch 5.50 GPH 60° at different water pressures measured at two different distances of the nozzle to the laser beam

A comparison of all nozzles and their droplets' mean diameters are displayed in Figure 15. The smallest droplets were measured at 5 bar and were generated by the DANFOSS 0.60 GPH 45° nozzle (61.86 μm). The biggest droplets at 5 bar were generated by the DANFOSS 5.50 GPH 45° nozzle (95.50 μm). As the pressure increased from 2.6 bar to 5 bar a sharp decrease in droplet size was observed. The DANFOSS 2.50 GPH 45° nozzle showed the biggest change in droplet size from 2.6 to 5 bar ($\Delta=75.31 \mu\text{m}$), while the droplet size of the Monarch 5.50 GPH 60° nozzle decreased only about 26 μm with increasing pressure.

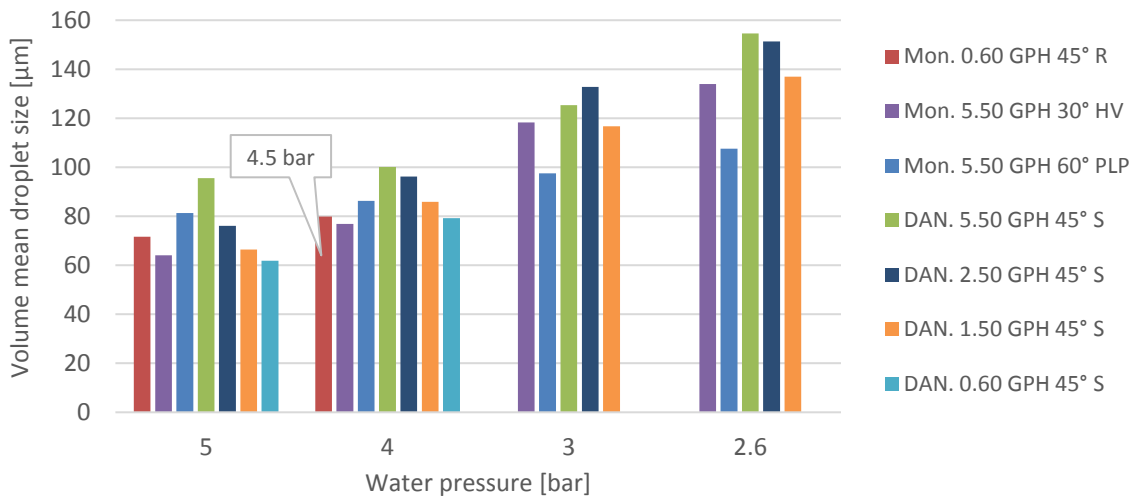


Figure 15: Mean diameter of spray droplets from 7 different nozzles at different water pressures measured with Malvern particle sizer at a nozzle-to-laser beam distance of 4 cm.

During all measurements the water temperature was between 20.8°C and 23.1°C. Comparing the droplet sizes of nozzles with a full cone spray pattern (see Figure 16), it can be observed that the nozzle with the highest flow rate (DANFOSS 5.50 GPH 45°) generated the biggest droplets. With a volume mean diameter of 61.86 µm the DANFOSS 0.60 GPH 45° nozzle generated the smallest droplets. From Figure 16 it can also be seen that there is a slight difference in the spray patterns of DANFOSS and Monarch nozzles, as the nozzles generated droplets with different sizes (61.86 µm vs. 71.65 µm) even though their flow rate and spray angle is the same (0.60 GPH and 45°).

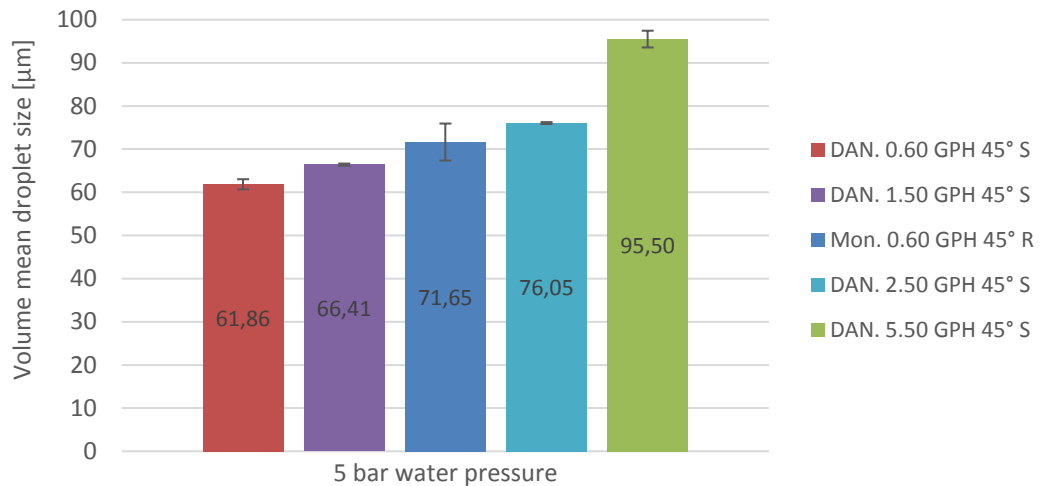


Figure 16: Mean diameter of spray droplets from spray nozzles with full cone spray pattern at 5 bar water pressure measured with Malvern particle sizer at a nozzle-to-laser beam distance of 4 cm.

6.1.3 Discussion

To keep the experiment rather simple and less time-consuming the nozzles were connected to the water tap in the laboratory. This restricted the experiment in two ways: for one, only lukewarm water (between 21°C and 23°C) was available from the water tap; and for another, the pressure was limited to around 5 bar. During the measurements, fluctuations in the pressure were observed, especially around 5 bar. It was also observed that droplet size slightly increased in cases where the laser beam was not passing exactly through the centre line of the spray cone.

The results of all measurements with a nozzle-to-laser beam distance of 4 cm are in agreement with the theory, showing that droplet size increases with decreasing pressure. The measurements with the Monarch 5.50 GPH 60° nozzle being 2 cm from the laser beam were first recorded at pressures of 4, 3.15, and 2.6 bar. When re-measuring the background it turned out that the optical unit had to be re-aligned. Therefore the measurements were repeated, this time at pressures of 5, 4, 3, and 2.6 bar. Since background scattering might have caused an increase in the droplet size, only the data of the second measurement run are presented in Figure 14. Overall, the Malvern particle sizer is a simple and fast instrument to measure droplet size distributions of sprays.

Because the properties of the Ca-rich solution are quite similar to those of water, droplet sizes in the same range as the measured ones can be expected for the spray carbonation experiments. With a slightly higher viscosity of the Ca-rich solution compared to water (1.11cP at 20°C [25]), a slight increase in droplet size can be expected.

6.1.4 Calculations Based on Experimental Results

With the data obtained from the size measurements the terminal velocity for droplets of each nozzle type was calculated. The velocity of the counter flowing CO₂ gas was estimated based on the stoichiometric volume flow rate and the cross sectional area of the gas pipe. The terminal velocity and the Reynolds number were calculated according to Eq.31 and Eq.32 respectively (see Chapter 5.1.1.1). Recommended correlations for the Reynolds number and the drag coefficient as stated in Table 7 were used to calculate the drag coefficient.

Table 9: Terminal velocity calculated for each nozzle based on the droplet size data obtained by the spray analysis (pressure = 5 bar)

Nozzle	Q [L/min]	d ₀ [mm]	u _e [m/s]	u _r [m/s]	d _d [μm]	Re	C _D	u _{td} [m/s]
Mon. 0.60 GPH 45° R	0.029	0.5	2.46	2.54	71.65	22.44	2.54	0.46
DAN. 5.50 GPH 45° S	0.270	0.8	8.95	9.65	95.50	113.78	1.02	0.83
Mon. 5.50 GPH 60° PLP	0.266	1.0	5.64	6.33	81.37	63.61	1.38	0.66
Mon. 5.50 GPH 30° HV	0.266	0.8	8.82	9.51	64.10	75.24	1.26	0.61
DAN. 0.60 GPH 45° S	0.029	0.5	2.46	2.54	61.86	19.37	2.77	0.41
DAN. 1.50 GPH 45° S	0.074	0.5	6.25	6.44	66.41	52.83	1.53	0.57
DAN. 2.50 GPH 45° S	0.123	0.5	10.42	10.74	76.04	100.82	1.08	0.72

From the droplet size of each nozzle it is also possible to give a rough estimation about the theoretical particle size of a PCC particle. The theoretical PCC particle size was estimated assuming that the size of a PCC particle is limited to the amount of calcium inside the droplet, since the molar ratios for Ca and CaCO₃ are 1:1. Consequently, a bigger droplet contains more Ca which can react with the CO₂ to create more CaCO₃ compared to a smaller droplet. It was further assumed that one litre of the solution contains 20 g of Ca. Once the mass of CaCO₃ is known, the volume can be calculated by its density (2.71 g/cm³). The following table presents the theoretical particle size of a cube-shaped PCC particle for each nozzle type based on the droplet size.

Table 10: Theoretical particle size of a cube-shaped PCC particle (V=volume; s=cube's side length)

Nozzle	d _{d (v,0.5)} [μm]	V _{CaCO3} [μm ³]	s _{cube} [μm]
Mon. 0.60 GPH 45° R	71.65	3 549.60	15.25
DAN. 5.50 GPH 45° S	95.50	8 405.06	20.33
Mon. 5.50 GPH 60° PLP	81.37	5 199.73	17.32
Mon. 5.50 GPH 30° HV	64.10	2 541.58	13.65
DAN. 0.60 GPH 45° S	61.86	2 284.12	13.17
DAN. 1.50 GPH 45° S	66.41	2 826.14	14.14
DAN. 2.50 GPH 45° S	76.04	4 243.19	16.19

6.2 Spray Carbonation Experiments

Due to delays with the construction of the test plant, the time for experimental work was limited and therefore it was decided to keep the focus of the experimental work rather on producing PCC with a certain particle size distribution than producing PCC with a certain morphology. The main challenges encountered during the experimental work are discussed in an additional section of this chapter (see section 6.2.4).

6.2.1 Equipment Setup

Figure 17 depicts the main elements of the equipment setup used for the spray carbonation experiments. The key components of the laboratory-scale test plant are summarized in Table 11.

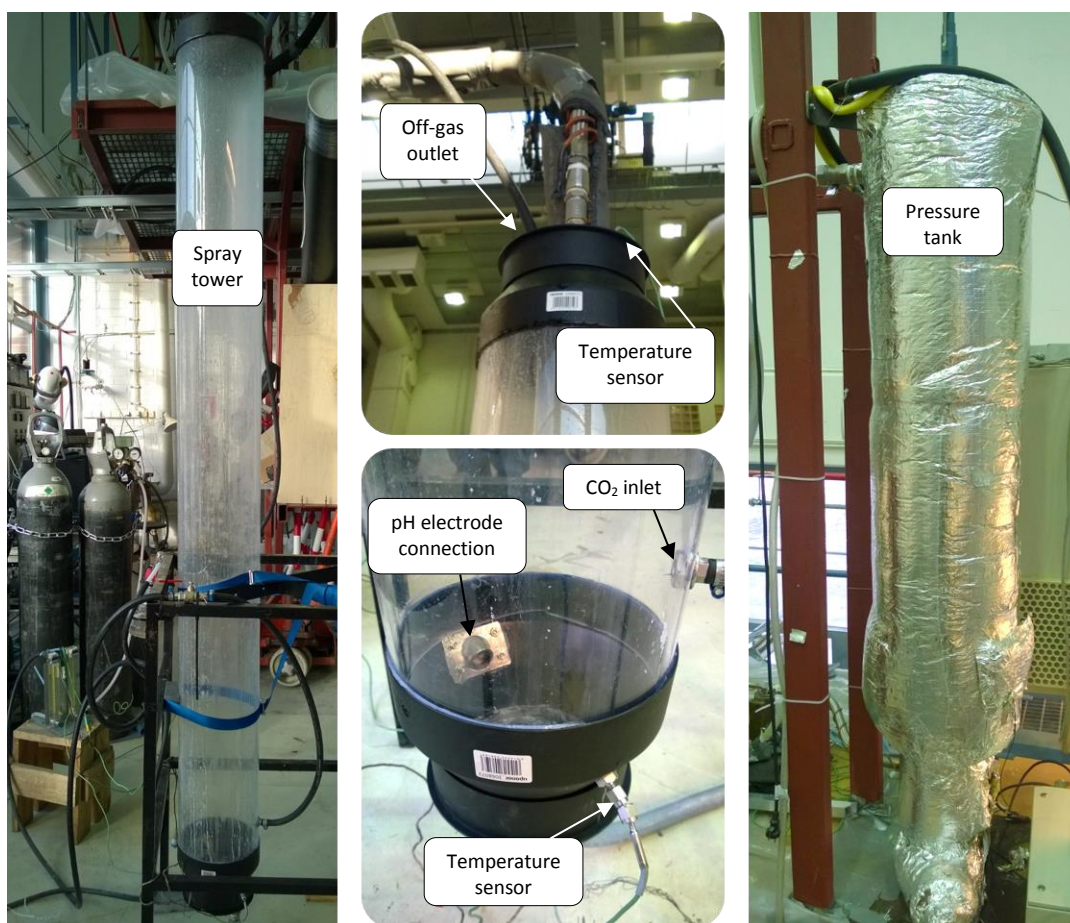


Figure 17: Spray tower and pressure tank of the laboratory-scale test plant

Table 11: Key components of the laboratory-scale test plant

Name	Number of units	Type/ Description
Pressure tank	1	Acid resistant steel; 100 L; max. 40 bar
Spray tower	1	Acrylic pipe; 200x194, 2m
Pump	1	SEF; MAG 33 T8; 0.35 kW; 50 Hz
Pipe	1	Acid resistant steel
Variable area flow meter	1	Kytölä Instruments, LH-5AR-HR; 0.5-7 NL/min
pH meter	1	JUMO tecLine pH single-rod electrode; pH 0-12
Temperature sensors	2	Type K thermocouple

6.2.2 Methodology

Before each test run all instruments were checked, all valves were closed, and the nozzle was assembled in the spray tower. The Ca-rich solution was then pumped into the pressure tank which was sealed and pressurized afterwards. Nitrogen gas was used to pressurize the tank. After that, the volumetric flow rate of CO₂ was adjusted and the spray tower was filled with CO₂ gas. Then the valve from the pressure tank to the spray tower was opened and Ca-rich solution was sprayed into the spray chamber. Depending on the test run the outlet pressure of the nitrogen cylinder was adjusted to 5 bar or 10 bar. The BenchLink Data Logger 3 was used to record temperature and pH in the spray tower. The produced PCC was collected after each test run and dried for 24 hours at 120°C. After each test run the spray tower was rinsed and cleaned with hot water and a brush.

Initially the focus of the experimental work was on the question whether it is possible to produce PCC with different spraying nozzles and if there are any significant changes in particle size distribution based on the nozzle type. The first tests were therefore performed with the Monarch 5.50 GPH 60°, Monarch 0.60 GPH 45°, and Monarch 5.50 GPH 30° nozzle. To study the effect of pressure on particle size distribution three tests at 10 bar were additionally performed with the DANFOSS 5.50 GPH 45° nozzle (Test 6), the Monarch 0.60 GPH 45° (Test 7) and the DANFOSS 2.50 GPH 45° nozzle (Test 11). After receiving the results from the particle size distribution analysis of the first three tests, it was decided to further investigate the correlation between the nozzle's capacity and the final particle size distribution. To do so, experiments with three nozzles with the same spray angle but different flow rates were performed (Test 8, 9 and 10). All test runs are summarized in Table 12.

Table 12: Run matrix for the laboratory-scale spray carbonation experiments

Test #	Tested Nozzle	Pressure [bar]	CO ₂ flow [L/min]	Stoich. CO ₂ flow [L/min]	Test duration [min]
Test 1	Monarch 5.50 GPH 60°	5	~ 9.5	3.24	37
Test 2	Monarch 0.60 GPH 45°	5	> 1	0.35	15
Test 3	Monarch 5.50 GPH 30°	5	> 1	3.24	10
Test 4	Monarch 5.50 GPH 30°	5	~ 2.5	3.24	11
Test 5	DANFOSS 5.50 GPH 45°	5	~ 3.5	3.28	8
Test 6	DANFOSS 5.50 GPH 45°	10	~ 4.5	4.52	9
Test 7	Monarch 0.60 GPH 45°	10	~ 2.0	0.48	40
Test 8	DANFOSS 0.60 GPH 45°	5	~ 2.0	0.35	30
Test 9	DANFOSS 1.50 GPH 45°	5	~ 2.0	0.90	18
Test 10	DANFOSS 2.50 GPH 45°	5	~ 2.0	1.49	16
Test 11	DANFOSS 2.50 GPH 45°	10	~ 3.0	2.06	15

It shall be mentioned that after Test 3 the CO₂ flowmeter was changed in order to enable a more accurate adjustment of the CO₂ volumetric flow rate. The Ca-rich solution that was used for the experiments was generated with the conventional X2PCC process and with a slag-to-liquid ratio of 100 g/L. The solution's calcium concentration is around 20 g/L.

To determine the particle size distribution (PSD) of the PCC particles the samples were taken to the Aalto University School of Chemistry, where they were tested with the Malvern Mastersizer 2000 (with a Hydro 2000MU wet sample dispersion unit). One feature of the Malvern Mastersizer 2000 is the variable power in-line sonication, which can help to break large agglomerates of particles. Each sample was tested three times. The first measurement

was recorded after letting the sample disperse in the deionized water for 2 minutes (no us). The second measurement was taken after applying ultrasound to the sample for 2 minutes (us on), and the third measurement 2 minutes after the ultrasound has been turned off (us off). The ultrasonic probe tip displacement indicator, which shows the power of the ultrasonic probe, was set to 5 μ for all measurements. Deionized water was used as dispersant (refractive index of 1.33) and the pump speed was set to 2500 rpm. The optical properties of the particles were defined with a particle refractive index of 1.52 and a particle absorption of 0.1.

Samples of the produced PCC were also sent to the Center of Microscopy and Nanotechnology in Oulu, Finland where the PCC morphology was determined by Scanning Electron Microscope (SEM) imaging and by X-ray diffraction (XRD analysis). The XRD analyses were performed using a Rigaku SmartLab 9 kW diffractometer. To identify crystalline phases the PDXL2 software was used and quantitative results were obtained via a Rietveld analysis.

6.2.3 Results & Discussion

The test results of the spray carbonation experiments are summarized in Table 13.

Table 13: Results for the spray carbonation experiments

Test #	t_{test} [min]	$\overline{\text{pH}}$	$\overline{T}_{\text{bottom}}$ [°C]	$\overline{T}_{\text{top}}$ [°C]	G/L [m ³ /L]	PCC particle size D (v, 0.5) [μ m]			Crystal morphology
						(no us)	(with us)	(us off)	
1	37	7.62	13.49	20.07	0.036	36.21	29.93	29.77	Calcite
2	15	8.13	n/a	19.82	0.034	22.86	20.68	21.24	Calcite
3	10	8.81	n/a	20.73	0.004	42.56	29.05	29.61	n/a
4	11	8.26	n/a	21.52	0.009	33.66	29.13	29.45	Calcite
5	8	7.95	17.56	21.16	0.013	43.44	38.57	38.25	Calcite
6	9	8.04	20.40	23.03	0.012	46.15	40.11	39.91	Calcite
7	40	7.81	15.91	19.96	0.050	29.29	24.41	25.90	Calcite
8	30	8.06	17.64	19.95	0.069	66.98	55.50	53.33	Calcite
9	18	8.24	17.98	20.52	0.027	53.70	43.20	42.28	Calcite
10	16	8.39	18.97	21.20	0.016	47.86	41.74	41.41	Calcite
11	15	8.20	19.80	22.87	0.018	57.55	47.96	47.06	Calcite

During each spray carbonation test the temperature in the bottom as well as in the top of the spray tower increased between 0.28°C and 4.64°C. Sudden temperature changes were measured during some of the test runs and were probably due to temperature changes inside the laboratory hall (caused by opening of doors in winter time). Due to a malfunction of one of the temperature sensors there are no data available for temperature measurements in the bottom of the spray tower for Test 2, Test 3, and Test 4. While the pH was strongly fluctuating in the beginning of most of the test runs, a more stable value was usually reached towards the end of each test run. However, since the pH electrode was not submerged in the solution for most of the time of the experiments, pH values are only conditionally representative. The highest end pH was reached during Test 3 (9.28) and the lowest during Test 6 (7.95). Charts illustrating the temperature and pH recordings of all experiments can be found from Appendix B.

The gas-to-liquid ratio (G/L ratio) defines the amount of cubic metre CO₂ used per litre of Ca-rich solution. Depending on the test run the G/L ratio ranged from 0.004 to 0.069 m³/L, when the calculated stoichiometric G/L ratio equals 0.012 m³/L.

Due to the similarities between Test 3 and Test 4, the XRD analysis and SEM imaging was only performed for the sample of Test 4. It is assumed that the polymorph of PCC from Test 3 is calcite as well. The effects of different parameters on the PSD and the morphology are discussed in more detail in the following pages.

6.2.3.1 Particle Size Distribution

Figure 18 shows the mean and standard deviations for the PSD of the measured PCC samples. The values include the data from all three measurement rounds (no us, us on, and us off). The smallest PCC particles were generated with the Monarch 0.60 GPH 45° nozzle both at 5 bar and at 10 bar (Test 2 and Test 7). Test 2 (us on) gave the smallest particle size of 20.68 µm. All experiments yielded PCC particles too coarse to be used directly as filler material in the paper or plastic industry.

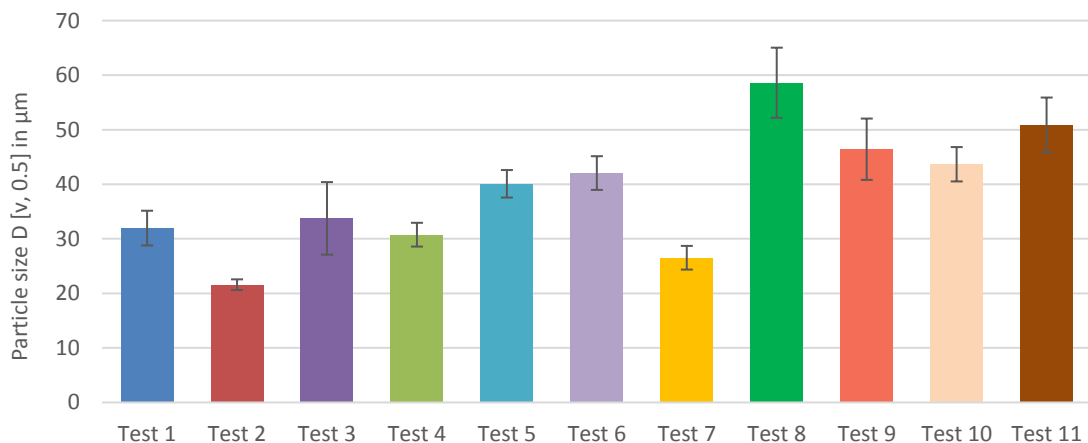


Figure 18: Result of PCC particle size measurements: mean particle size and standard deviation

Interestingly, all tests performed with the Monarch nozzles (Test 2, Test 7, Test 4, Test 1, and Test 3) generated smaller particles compared to tests using DANFOSS nozzles. Only when analysing the test results it was noticed that a change in the methodology might have been responsible for the bigger particle size values of Test 8, 9, 10, and 11. The cleaning and brushing of the spray tower was usually very time consuming compared to the actual duration of the spray carbonation test. Because Test 8, 9, 10, and 11 were all performed on the same day, the spray tower wall was not brushed after each test run, as otherwise customary. In order to save time, the spray tower was only rinsed with water between each test run. The rinsing water, containing PCC particles that were washed from the spray tower wall, was then collected together with the PCC rich solution. In previous experiments only PCC rich solution that had been accumulated at the bottom of the spray tower was collected and any PCC particles left on the spray tower wall were lost during the cleaning of the reactor. It is likely that these deposited PCC particles caused an increase of the average PSD, as it will be discussed in more detail later.

A complete table with the results of the PSD measurements for the PCC samples can be found from Appendix C. All tests show a mono-modal particle size distribution with a peak

shift towards a smaller particle diameter after the application of ultrasound. On an average the particle size of all samples could be decreased by 7 μm with the help of ultrasonic treatment. The particle size of some samples decreased even further with the third measurement, while other samples' particle size increased slightly as soon as the ultrasound was turned off. When comparing the measured $D(v, 0.9)$ particle sizes before and after the application of ultrasound (see Table 14), it can be seen that the $D(v, 0.9)$ of all tests, except Test 2, has been bigger before the ultrasound application. In the case of Test 2 the $D(v, 0.9)$ particle size decreased by 17% with the application of ultrasound, but increased again by 18% after the ultrasound was turned off.

Table 14: Decrease of $D(v, 0.9)$ particle size - compared before and after the application of ultrasound

Test #	1	2	3	4	5	6	7	8	9	10	11
$\Delta D(v, 0.9)$	36%	-2%	165%	16%	25%	33%	19%	91%	52%	25%	30%

To emphasize the effect of ultrasonic treatment on PSD an additional measurement with increased ultrasonic power was recorded; the sample of Test 8 was measured without the application of ultrasound, once with ultrasound with an ultrasonic displacement indicator of 5 μ , and once with ultrasound with an ultrasonic displacement indicator of 10 μ . As a result, the particle size decreased from 66.98 μm (no us) to 55.50 μm (us on 5) to 46.09 μm (us on 10). The PSD of two samples (Test 5 and Test 8) before, with, and after the application of ultrasound is shown in Figure 19 for comparison. It can be seen that the PSD of Test 5 is very symmetric without any minor peaks before as well as after the application of ultrasound. In the sample of Test 8 on the other hand, the occurrence of agglomerates is clearly visible in the form of a peak at around 500 μm . A longer ultrasound application may have broken these agglomerates even further, this was however not investigated.

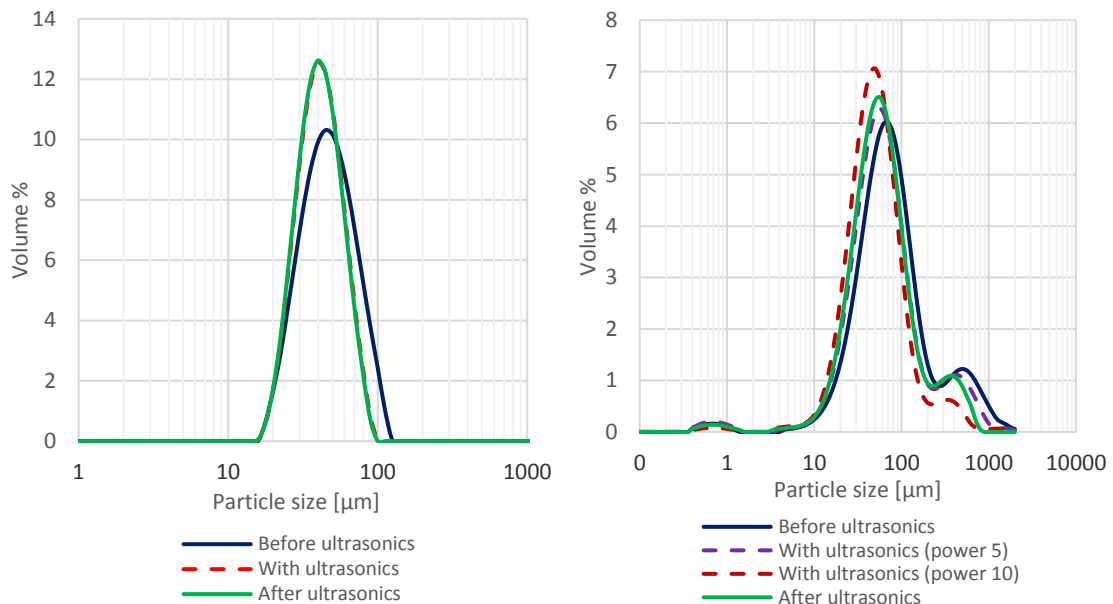


Figure 19: PSD of Test 5 (left) and Test 8 (right) before, with and after the application of ultrasound

Figure 20 illustrates the difference in PSD of two spray carbonation samples and two samples from experiments with the conventional X2PCC plant. The mean particle size of Test 2 is around 11 μm and 14 μm smaller compared to Test 4 X2PCC and Test 9 X2PCC

respectively. On the other hand, the mean particle size of Test 8 is around 21 μm bigger compared to Test 4 X2PCC and 18 μm bigger compared to Test 9 X2PCC.

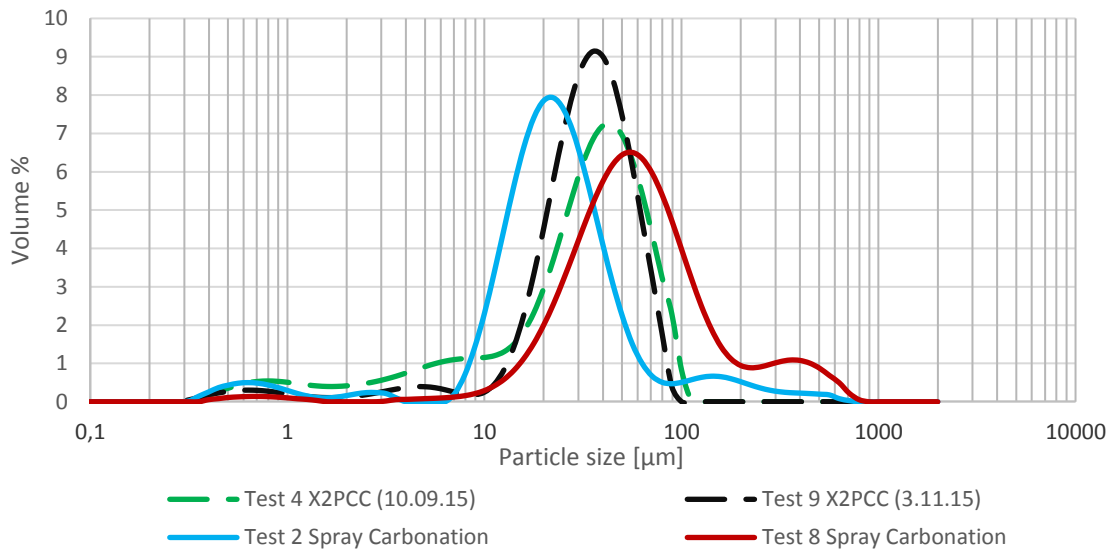


Figure 20: Comparison of PSD (after ultrasound) between samples of spray carbonation tests (Test 2 and Test 8) and conventional X2PCC carbonation tests (Test 4 X2PCC and Test 9 X2PCC)

Effect of droplet size on particle size

Earlier in this work the theoretical particle size of a PCC particle was estimated based on the amount of calcium inside a droplet. The calculations predicted that the side length of a cube-shaped PCC particle from a droplet with a diameter of about 70 μm would be around 15 μm . Figure 21 compares the PCC mean particle size (after us) with the mean droplet size from different nozzles and the theoretical PCC particle size. The sample of Test 2 has the smallest deviation of the measured PCC particle size from the theoretical particle size, while the sample of Test 8 shows the maximum deviation (40 μm) from the theoretical particle size.

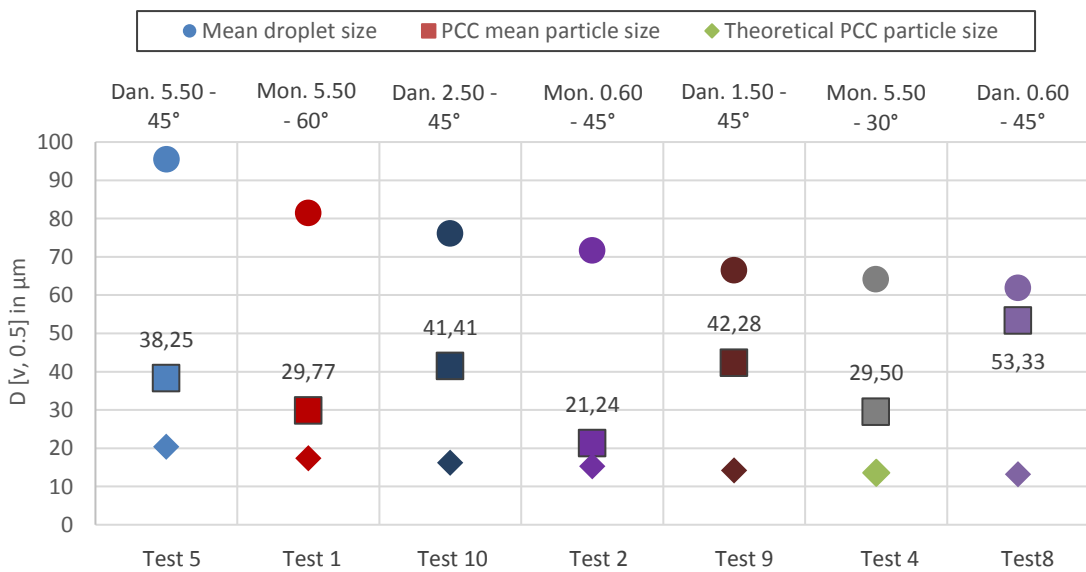


Figure 21: Comparison of droplet diameter, PCC particle size (after us) and theoretical PCC particle size (side length of cube-shaped particle)

Figure 22 shows the PCC particle size as a function of the droplet size. Given the data depicted in both graphs, it can be seen that in all cases the particle size is smaller than the droplet size. However, there is no clear trend confirming that nozzles with smaller droplets also create smaller PCC particles. When analysing these and also the following results, it should be kept in mind that agglomeration has a great impact on the outcome of this study. If the precipitation reaction does not happen fast enough, one can also assume that droplets will first collide with each other or deposit on the spray tower wall and finally on the bottom, which would mean that the original droplet size had already changed before the precipitation happens. Furthermore, higher flow rates cause more turbulent spray patterns, which in turn favour the deposition of droplets on the spray tower wall, especially in the area where the spray projects to the wall.

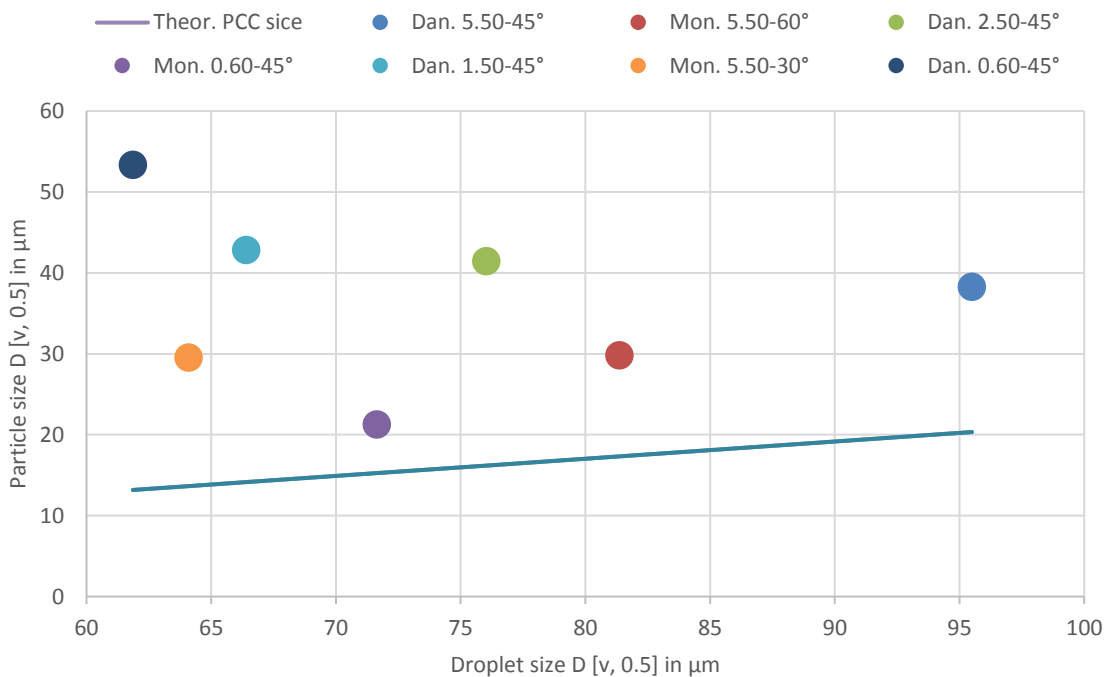


Figure 22: Actual and theoretical PCC particle size vs. droplet size

Effect of spray angle on particle size

To study the effect of different spray angles on the particle size, nozzles with the same flow rate but with different spray angles were tested (Monarch 5.50 GPH 60°, Monarch 5.50 GPH 30°, and DANFOSS 5.50 GPH 45°). All four tests were conducted at a pressure of 5 bar. Before conducting the experiments it was expected that with a narrower spray angle fewer droplets will collide with the tower wall and that the nozzle with the narrowest spray angle will generate the smallest PCC particles. The results show that the nozzles with 60° and 30° spray angle generated PCC particles of almost the exact same size whereas the nozzle with a spray angle of 45° clearly generated bigger PCC particles (see Figure 23). The tall and slim design of the spray tower may be responsible for these results. Since the diameter of the spray tower is only 200 mm collisions of droplets against the spray tower wall were unavoidable, even when using a nozzle with a 30° spray angle. Differences in the design of Monarch and DANFOSS nozzles may as well cause variations in particle sizes. To indicate whether the nozzle design is responsible for the differences in the particle size, further experiments with nozzles not only with the same capacity but also made by the same manufacturer would be needed.

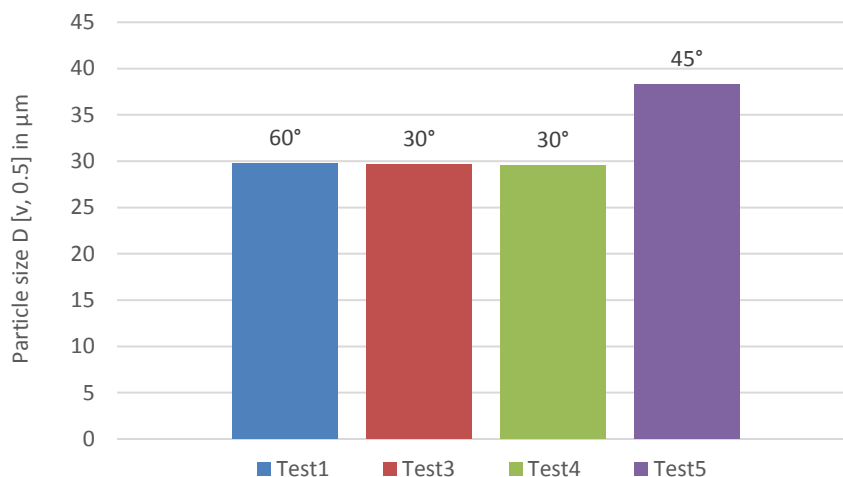


Figure 23: Comparison of PCC particle size of spray carbonation tests with nozzles with same flow rate (5.50 GPH) but different spray angles (60°, 45°, and 30°)

Effect of nozzle capacity on particle size

To determine whether the nozzle capacity has an effect on the particle size, four DANFOSS nozzles with a spray angle of 45° and a capacity of 0.60 GPH, 1.50 GPH, 2.50 GPH, and 5.50 GPH were tested. The effect of different nozzle capacities on the particle size is shown in Figure 24. While the nozzle with the highest capacity produced the smallest particles, the nozzle with the lowest capacity produced the biggest particles.

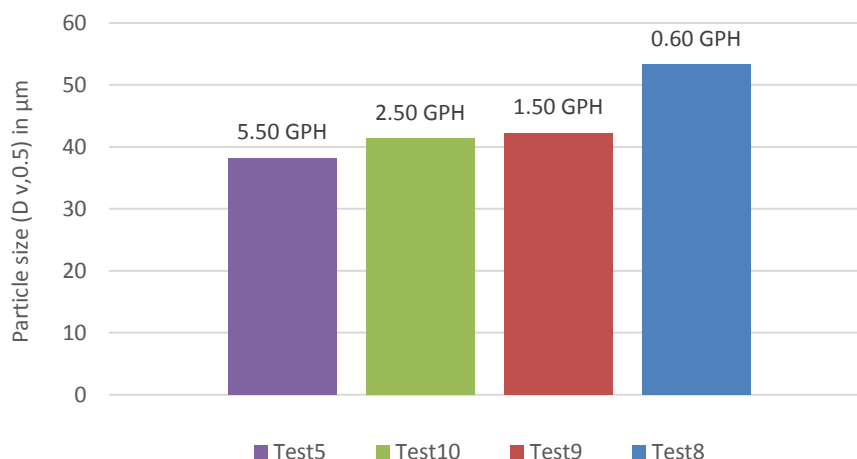


Figure 24: Comparison of PCC particle sizes of spray carbonation tests with DANFOSS nozzles with a spray angle of 45° and varying flow rates

The illustrated results are somewhat inconsistent with the before discussed hypothesis, that a higher flow rate would cause more collisions and therefore have a negative impact on the PCC particle size (in terms of bigger particles). One explanation for the shown correlation between nozzle capacity and particle size could be that experiments with a small nozzle capacity last longer, and therefore increase the probability for crystal growth and formation of agglomerates. When looking at the G/L ratio of Test 5, 10, 9, and 8 a trend between the G/L ratio and the particle size can be observed: With increasing G/L ratio the particle size increases. While the actual CO₂ flow rate during Test 5 was close to the stoichiometric value,

the actual CO₂ flow rate during Test 8 was almost 6 times higher than the stoichiometric flow rate.

Effect of pressure on particle size

It has been assumed that an increase in pressure will cause the droplet size to decrease and consequently also the PCC particle size to reduce. The results of the PSD measurements reveal, contrary to expectations, that an increase in pressure causes an increase in the PCC particle size. As shown in Figure 25 each nozzle (DANFOSS 5.50 GPH 45°, Monarch 0.60 GPH 45°, and DANFOSS 2.50 GPH 45°) produced bigger PCC particles at 10 bar pressure than at 5 bar pressure. Increasing the pressure from 5 bar to 10 bar clearly increased the impact of the droplets on the spray tower wall. A very turbulent fine spray mist was produced by the nozzle creating a foggy area around the nozzle head and in the upper part of the tower. Due to the lower flow rate during Test 7 and 11 the spray tower wall first seemed to be less wet compared to Test 6. As the experiments proceeded, depositions started to build up on the tower wall, especially in the upper part of the spray tower. The longer the experiments took, the wetter the wall also became. For example, during Test 6 it was clearly visible that PCC particles were running down the wet tower wall to the bottom of the spray tower. During all experiments it was also noticed that turbulent spray pattern only occur –if they occur– in the upper part of the spray tower. When observing the lower part of the tower, one could see particles falling steadily to the bottom of the spray tower, where they accumulated in the spraying solution. Particles that deposited on the spray tower wall, on the other hand, stayed in direct contact with the CO₂ gas stream. During the experiments the solution containing the PCC particles was drained from the spray tower from time to time. That implies that deposited particles spent longer time in the spray tower compared to particles which fell to the spray tower bottom.

By looking at the results presented in Figure 25 and considering the experimental observations, it seems plausible that the mean particle size is larger in cases with turbulent spray pattern, as higher fluid pressure causes deposition of droplets on the tower wall.

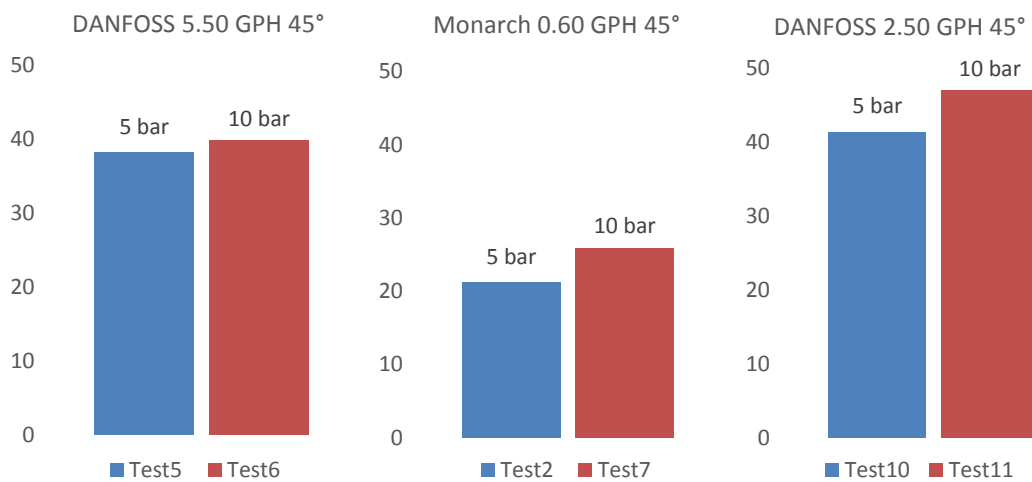


Figure 25: Comparison of average PCC particle size ($D [v, 0.5]$ in μm) of spray carbonation tests with 5 and 10 bar

6.2.3.2 Morphology

Table 15 presents the results of the morphology analysis including the outcome of the quantitative phase identification. Calcite has been identified as the major component for all the tested samples. With 96.59% Test 6 has the highest calcite content, while Test 5 has the lowest one with 80.48%. Calcium titanium iron (III) oxide has been identified as a minor component in most of the test samples (1, 2, 4, 6, 7, 8, 10, and 11). Other minor components discovered are magnesium fluoride, sodium peroxide, chabazite, chromium oxide, graphite, perovskite, silicon oxide hydrate, and sodium magnesium.

Table 15: Results of the morphology analysis of samples from the spray carbonation experiments

Test #	t _{Test} [min]	CO ₂ flow [L/min]	Stoich. CO ₂ flow [L/min]	G/L [m ³ /L]	PCC size (no us) [μm]	Crystal morphology	[CaCO ₃] [%]	[Others] [%]
1	37	~ 9.5	3.24	0.036	36.21	Calcite	96.10	3.90
2	15	> 1	0.35	0.034	22.86	Calcite	94.30	5.70
4	11	2.5	3.24	0.009	33.66	Calcite	96.10	3.90
5	8	3.5	3.28	0.013	43.44	Calcite	80.48	19.52
6	9	4.5	4.52	0.012	46.15	Calcite	96.59	3.41
7	40	2.0	0.48	0.050	29.29	Calcite	90.21	9.79
8	30	2.0	0.35	0.069	66.98	Calcite	92.87	7.13
9	18	2.0	0.90	0.027	53.70	Calcite	96.40	5.60
10	16	2.0	1.49	0.016	47.86	Calcite	85.60	14.40
11	15	3.0	2.06	0.018	57.55	Calcite	92.61	7.39

The SEM images obtained from the morphology analysis are presented in Figures 26-30. By looking at the pictures, the rhombohedral, but agglomerated, nature of the particles produced can be confirmed. The images of Test 4 (see Figure 27) present what looks like to be the least agglomerated and most distinct rhombohedral crystals of around 10 μm in size. At the same time, the actual CO₂ flow rate during Test 4 was lower than the calculated stoichiometric CO₂ flow rate, meaning that the availability of CO₂ was limited. The CO₂ flow rate during all other experiments was either equal to or higher than the stoichiometric flow rate. This would suggest that a low G/L ratio favours the growth of rhombohedral faces in a less agglomerated state.

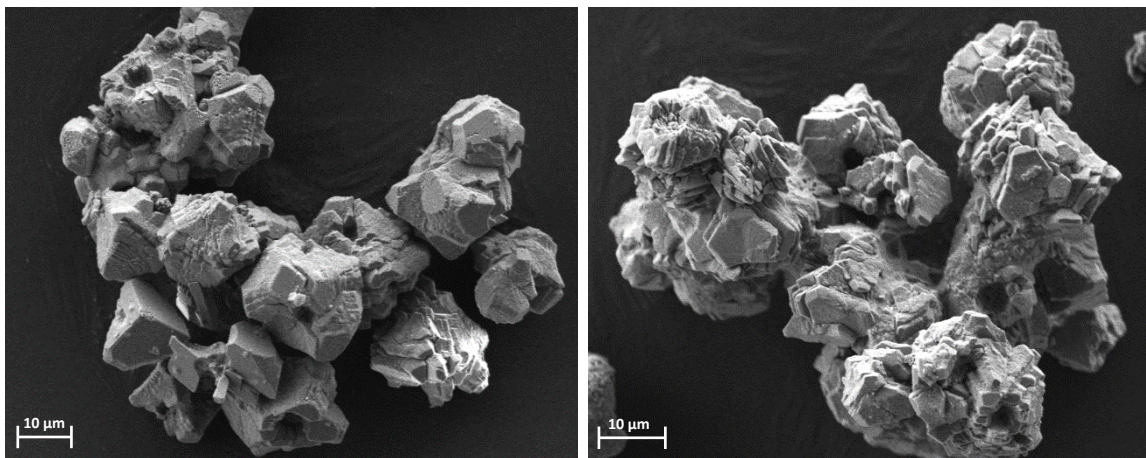


Figure 26: SEM images of samples from Test 1 (left) and Test 2 (right)

A long chain of single crystals forming one big particle can be seen in the left picture in Figure 29. This could explain why the PSD of the sample from Test 8 was much bigger compared to others.

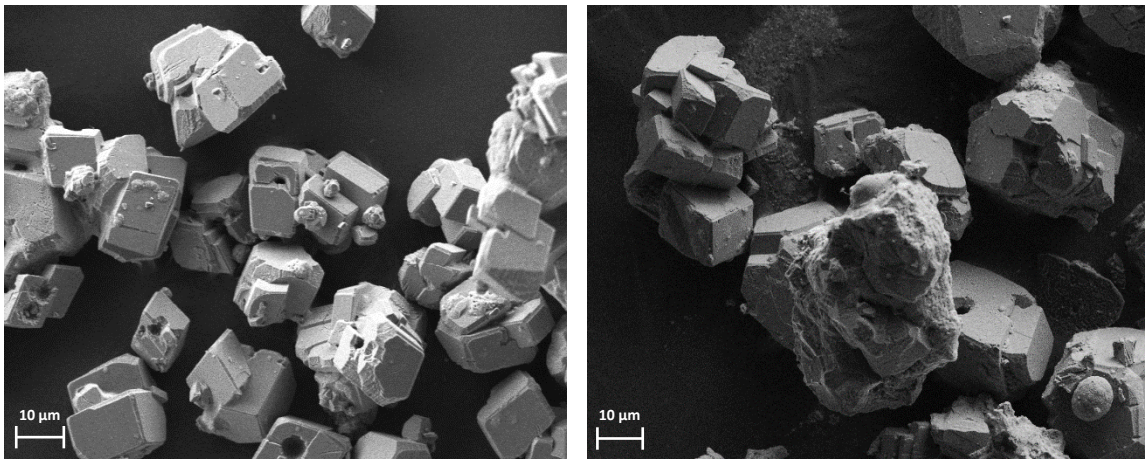


Figure 27: SEM images of samples from Test 4 (left) and Test 5 (right)

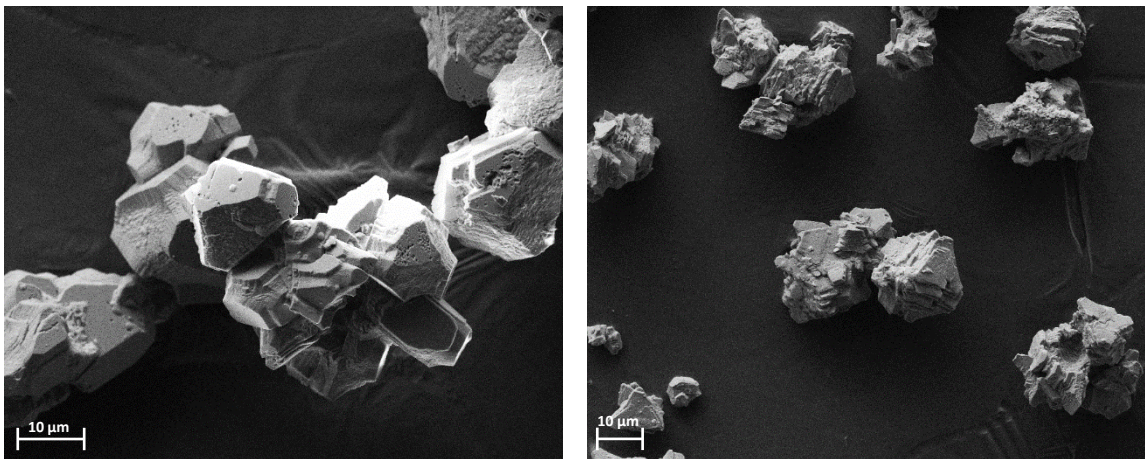


Figure 28: SEM images of samples from Test 6 (left) and Test 7 (right)

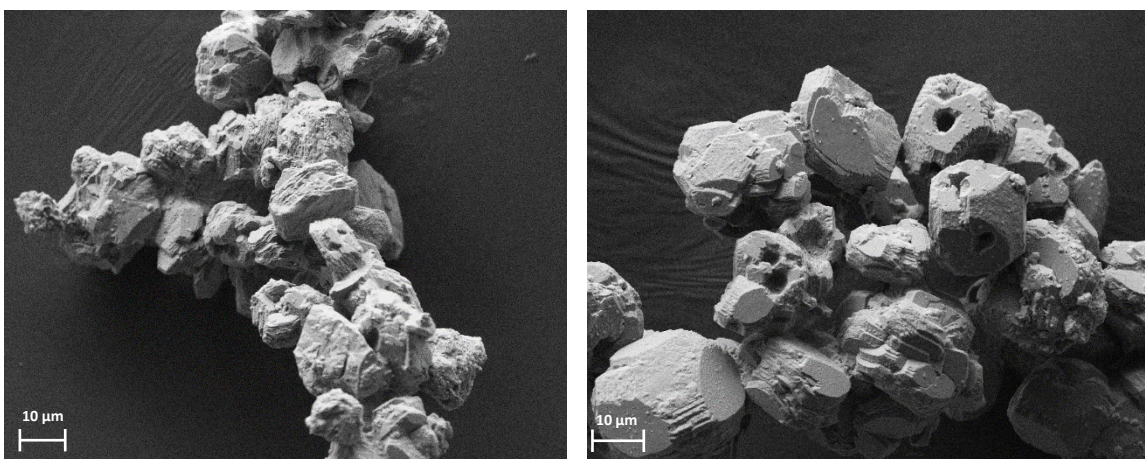


Figure 29: SEM images of samples from Test 8 (left) and Test 9 (right)

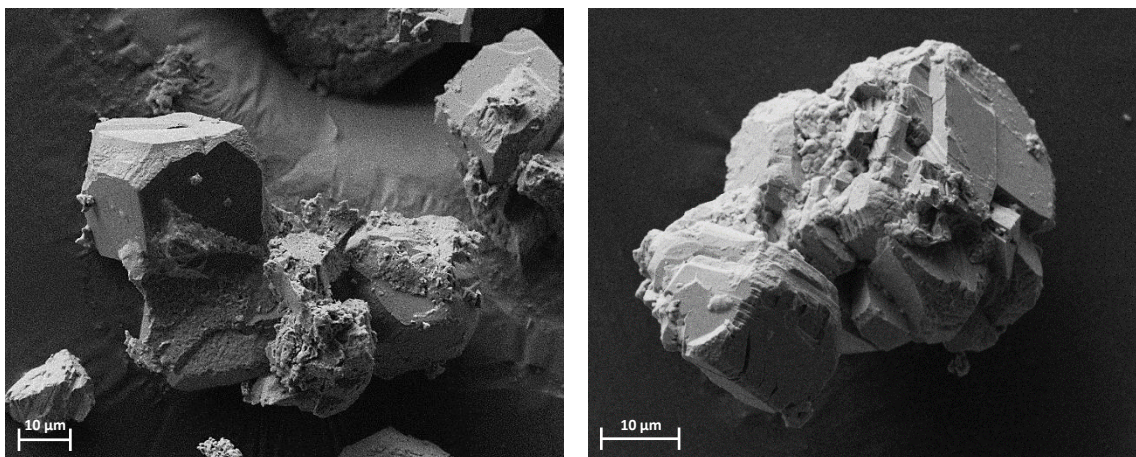


Figure 30: SEM images of samples from Test 10 (left) and Test 11 (right)

6.2.4 Experimental Learning and Challenges

This part of the work highlights some learnings and the main challenges encountered during the experimental work with the laboratory-scale test plant.

Spray tower design

One important criteria for the spray tower was the visibility into the tower. For the diameter of the acrylic pipe the maximum available size (20 cm) was chosen. Originally, the idea was to clean the spray tower after each experiment by filling it up with water (and if necessary adding 0.5 molar hydrogen chloride solution) and leaving it appeal overnight. The spray tower bottom, however, was not capable of handling the increasing mass of water inside the tower while filling it up, which caused a major leakage and a lasting damage to the seals of the bottom part of the tower. It was therefore decided to replace the complete bottom of the spray tower, which caused a delay of more than two weeks. By gluing the new bottom part and the bottom lid to the spray tower pipe, the problem of leakages would have probably been solved entirely. But since the spray tower had to be flushed and cleaned after each test run, it was decided to attach the lid with a rubber seal instead, which allowed to remove the bottom lid when necessary. Additionally it was decided to clean the tower with a brush instead of completely filling it up with water. To avoid or minimize leakages from the rubber seal during experiments, part of the PCC-rich solution was continuously drained from the tower. This had the disadvantage that the solution level in the bottom of the tower very rarely reached such a height that the pH electrode would have been emerged in the solution.

A problem was also encountered with the new thread for the pH electrode, as it was not 100 percent tight which caused gas leakages during some of the experiments.

Because of the fixed location of the pressure tank and the tall design of the spray tower, the bottom of the spray tower almost reached to the floor which made draining of the solution form the spray tower rather unhandy.

When testing nozzles with different spray angles it became apparent that collisions of droplets against the tower wall occurred even with a spray angle of 30°. One option to avoid these collisions could be to use a spray tower with a larger diameter.

Wear of nozzle

During the replacement work of the spray tower bottom, the Monarch 5.50 GPH 60° nozzle was left in the spray tower. In the course of a bit more than two weeks the nozzle became clogged and part of the filter material of the nozzle seemed to have oxidized (see picture 2 in Figure 31). To minimize the risk of plugging and oxidization for coming experiments, each nozzle was removed from the spray tower and cleaned after the experiment. Even though these precautions were taken, it still happened that after Test 7 the Monarch 0.60 GPH 45° nozzle became so clogged that any efforts to clean and reuse it for another experiment were ineffective. During Test 8 and 9 oxidization of the nozzle occurred even during the test run (see picture 3 in Figure 31). This caused also a discoloration of the PCC rich solution from white to a grey bluish colour. The nozzle filters of the DANFOSS 0.60 GPH 45° and the DANFOSS 1.50 GPH 45° nozzle are different than those from the DANFOSS nozzles with a higher capacity. It is likely that the difference in the filter material is responsible for the fast oxidization during Test 8 and 9.

The first picture in Figure 31 illustrates the importance of the nozzle filter. It shows the amount of dirt particles that were filtered during Test 5 and Test 6. Without the nozzle filter these particles would clog the nozzle orifice immediately.

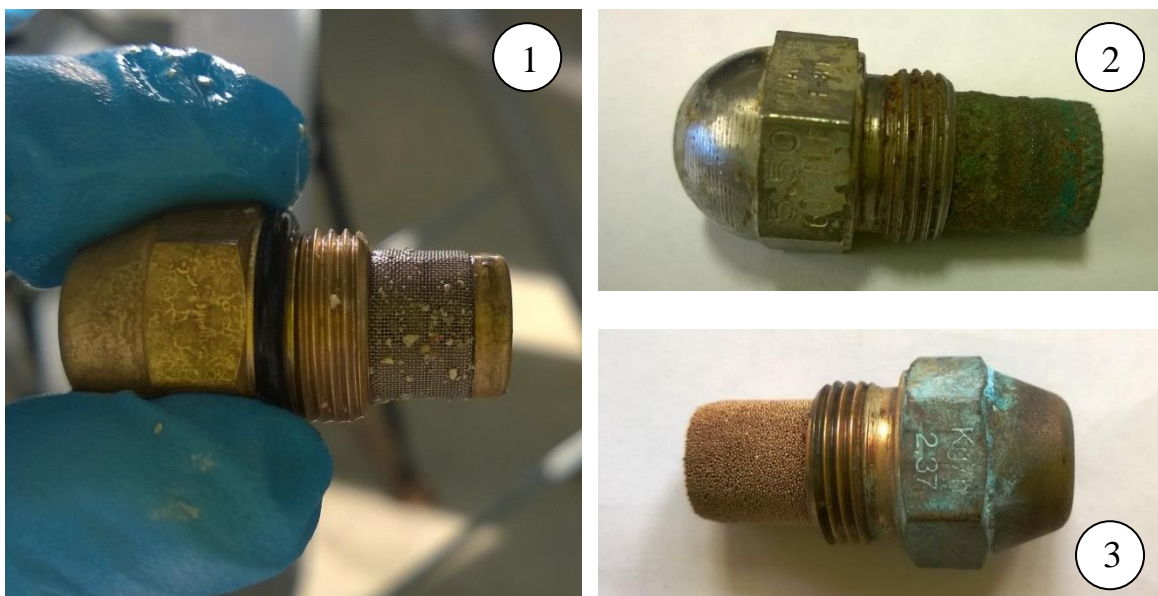


Figure 31: Picture showing dirt particles on the nozzle filter (1); PCC depositions on the Monarch 5.50 60° nozzle (2); oxidized DANFOSS 0.60 GPH 45° nozzle (3)

Filling the pressure tank

Using a pump to fill the pressure tank with the Ca-rich solution allowed to accelerate the filling process. However, the closed design of the pressure tank also posed the risk to overfill the tank and spill Ca-rich solution.

Measurements

The laboratory-scale test plant was originally equipped with a mass flow meter (Schlumberger DATAMATE 2100™) and a pressure meter to measure the flow rate and pressure of the Ca-rich solution entering the spray tower. Because the actual flow rate was too small for the mass flow meter to measure, no data about the liquid mass flow were

recorded during the experiments. Failure of the pressure meter also led to a lack of pressure measurement data for all the experiments. The liquid pressure was regulated with the pressure gauge from the nitrogen cylinder.

To study how much of the CO₂ actually undergoes a reaction to form PCC in the spray tower, it would also be necessary to measure the CO₂ concentration before and after the spray tower as well as the volumetric flow rate of the gas. Because it was not known how much nitrogen from the pressure tank ends up in the spray tower, it was not possible to affiliate the amount of gas bubbles in the off-gas scrubber to the amount of CO₂ gas leaving the spray reactor.

7 Conclusion

The objective of this work was to study the concept of a spray carbonation process with the aim to produce PCC from steelmaking slag and carbon dioxide. In order to determine whether it is possible to generate PCC via spray carbonation, a laboratory-scale test plant was designed and constructed. The spray carbonation test plant uses a spray nozzle to disperse fine droplets of a Ca-rich solution into a spray tower, where calcium carbonate precipitates as a result of the reaction between calcium and the counter flowing CO₂ gas. In addition to the spray carbonation experiments with the laboratory-scale test plant, also a spray analysis was conducted.

The feasibility of PCC production from steel slag via spray carbonation was successfully demonstrated at the laboratory-scale. All experiments succeeded in producing PCC in the form of rhombohedral calcite. The highest calcite content measured was 96.59 %. Depending on the extent of particle agglomeration, the PCC particle size ranged from 22.86 to 66.98 µm. Agglomeration was observed in all samples to a variable extent, which became also apparent when applying ultrasound to the samples. The results obtained from the spray carbonation experiments did not indicate that smaller droplet size leads to smaller PCC particle size. Furthermore, no correlation between different nozzle spray angles and particle size was observed. Yet, a trend between the G/L ratio and the particle size was seen when testing nozzles with the same spray angle but different capacities. In fact, the particle size increased with increasing G/L ratio. This seems reasonable considering that the crystal can continue to grow longer, the more CO₂ there is dissolved in the solution. Experiments with a fluid pressure of 10 bar revealed that a turbulent spray pattern favours the formation of big PCC particles. Droplet collisions and depositions on the spray tower wall were found to play an important role in this context.

When comparing the presented spray carbonation process with the conventional X2PCC process, it can be concluded that by using a spray nozzle instead of a gas sparger the PCC particle size can be decreased. Using a spray nozzle also resulted in a significant increase of the interfacial area between liquid droplets and the gaseous atmosphere, which enhances the mass transfer between the phases. The nozzles tested in this study produced droplets in a size range of 50 to 100 µm (at 5 bar). Different nozzles may generate even smaller droplets, which should be kept in mind in future research. A significant drawback of the spray carbonation process over the X2PCC process is the process capacity. Even though the precipitation reaction in the spray tower is very fast, the total carbonation time is much longer compared to the original X2PCC process. While the carbonation of 170 litres Ca-rich solution in the conventional X2PCC process takes about 30 minutes, it would take between 10 and 155 hours (depending on the nozzle capacity) to spray the same amount of solution into the spray tower. A bigger reactor and a nozzle with a higher capacity, or multiple nozzles would be needed to reduce the carbonation time of the spray carbonation process.

Even though the particle size of PCC crystals produced via spray carbonation is not yet of commercial standard, future research in this area seems very promising. While this study revealed a potential alternative to the conventional X2PCC process, more research is still needed to gain better insight into the reaction mechanisms and to obtain more knowledge how different parameters affect PSD and crystal morphology.

8 Recommendations

Based on the results of this thesis and on learnings from conducting the experimental studies, several recommendations for future research have been made and are presented in this section.

- Tests should be repeated in order to confirm the validity of their results. To gain a deeper understanding of the effect of certain parameters on the PCC particle size and morphology, only one test parameter should be changed at a time.
- Based on the challenges that were encountered during the spray carbonation experiments, it is recommended to design a spray tower with as few openings as possible since each opening or removable part poses a risk for leakages and should therefore be avoided. Other recommendations include measures to improve the handiness and operational safety of the plant. Due to the closed design of the pressure tank it was impossible to see how full or empty the tank was, which made the filling and pressurizing procedure more complicated. Also leaving more space between the spray tower bottom and the floor would increase the handiness when draining the solution from the spray reactor.
- It was hypothesized that droplet collisions and depositions on the spray tower wall and bottom are leading to bigger particle sizes. Further tests should be performed to determine whether a reduction in PCC particle size can be achieved by changing the spray tower design. Another option could be to come up with a spray tower design that allows to remove PCC particles from the spray tower as soon as precipitation has occurred. By quickly taking the PCC particles from the reactor, crystal growth may be arrested.
- Only Monarch and DANFOSS oil nozzles were used for the experiments in this study. More experiments with other nozzles should be performed in order to investigate whether it is possible to further decrease the droplet size and thereby also the PCC particle size.
- One challenge encountered during the experiments was oxidation of some of the nozzles. Nozzles with brass filter screens should therefore be avoided.
- Due to time constraints and delays in commissioning of the laboratory-scale plant no experiments at temperatures above room temperature were conducted. Additional experiments should be performed to study the effect of temperature on PCC morphology and to assess other parameters that have an influence on PCC morphology. To avoid any sudden temperature changes, such as the ones observed during the spray carbonation experiments, the ambient temperature should be kept constant.
- The application of ultrasound showed that some samples were strongly agglomerated. To get more insight into the ability of ultrasound to break agglomerates, measurements with longer ultrasound applications should be recorded.

- In order to determine how much of the incoming CO₂ actually undergoes a reaction in the spray tower, it is recommended to measure the CO₂ concentration before and after the spray tower as well as the volumetric flow rate of the gas.

References

- [1] Said, A., Laukkanen, T., and Järvinen, M., 2016, "Pilot-Scale Experimental Work on Carbon Dioxide Sequestration Using Steelmaking Slag," *Appl. Energy*, **177**, pp. 602–611.
- [2] Zappa, W., 2014, "Pilot-Scale Experimental Work on the Production of Precipitated Calcium Carbonate (PCC) from Steel Slag for CO₂ Fixation," Aalto University.
- [3] Teir, S., Eloneva, S., Fogelholm, C.-J., and Zevenhoven, R., 2007, "Dissolution of Steelmaking Slags in Acetic Acid for Precipitated Calcium Carbonate Production," *Energy*, **32**(4), pp. 528–539.
- [4] EuLA, 2014, *A Competitive and Efficient Lime Industry*, Belgium.
- [5] Stork, M., Meinderstma, W., Overgaag, M., and Neelis, M., 2014, *A Competitive and Efficient Lime Industry, Cornerstone for a Sustainable Europe (Lime Roadmap)*, Ecofys.
- [6] Said, A., Mattila, H.-P., Järvinen, M., and Zevenhoven, R., 2013, "Production of Precipitated Calcium Carbonate (PCC) from Steelmaking Slag for Fixation of CO₂," *Appl. Energy*, **112**, pp. 765–771.
- [7] Teir, S., Eloneva, S., Revitzer, H., Zevenhoven, R., Fogelholm, C.-J., and Pöylyö, E., 2009, "Menetelmä Kalsiumkarbonaatin Tuottamiseksi Jäte- Ja Sivutuotteista.", FI 122348 B
- [8] Gao, F., 2012, *Advances in Polymer Nanocomposites - Types and Applications*, Woodhead Publishing Limited.
- [9] Stratton, P., 2012, "An Overview of the North American Calcium Carbonate Market" [Online]. Available: <https://roskill.com/wp/wp-content/uploads/2014/11/download-roskills-paper-on-the-north-american-calcium-carbonate-market.attachment1.pdf>. [Accessed: 11-Nov-2016].
- [10] Minerals Technologies, n.d., "What Is PCC — Precipitated Calcium Carbonate?" [Online]. Available: [http://www.mineralstech.com/Pages/SMI/Precipitated-Calcium-Carbonate-\(PCC\).aspx](http://www.mineralstech.com/Pages/SMI/Precipitated-Calcium-Carbonate-(PCC).aspx). [Accessed: 20-Oct-2016].
- [11] Mattila, H.-P., and Zevenhoven, R., 2014, "Production of Precipitated Calcium Carbonate from Steel Converter Slag and Other Calcium-Containing Industrial Wastes and Residues," *Advances in Inorganic Chemistry*, Elsevier Inc., pp. 347–381.
- [12] Ghumare, N., 2015, "Paper Industry to Drive Global Calcium Carbonate Market to US\$25.01 Billion by 2019: Transparency Market Research," *Transpar. Mark. Res.*
- [13] Global Industry Analysts, 2015, "Calcium Carbonate Market Trends" [Online]. Available: http://www.strategyr.com/MarketResearch/Calcium_Carbonate_Market_Trends.asp. [Accessed: 14-Nov-2016].
- [14] Bajpai, P., 2015, "Pulp and Paper Chemicals," *Pulp and Paper Industry - Chemicals*, Elsevier, pp. 103–106.
- [15] Baek, C. S., Cho, K. H., and Ahn, J.-W., 2014, "Effect of Grain Size and Replacement Ratio on the Plastic Properties of Precipitated Calcium Carbonate Using Limestone as Raw Material," *J. Korean Ceram. Soc.*, **51**(2), pp. 127–131.
- [16] Reinste Nano Ventures, n.d., "Nano Precipitated Calcium Carbonate (NPCC) for Plastic Industry."
- [17] Mattila, H.-P., 2014, "Utilization of Steelmaking Waste Materials for Production of Calcium Carbonate (CaCO₃)," Åbo Akademi University.

- [18] Domingo, C., Loste, E., Gómez-Morales, J., García-Carmona, J., and Fraile, J., 2006, "Calcite Precipitation by a High-Pressure CO₂ Carbonation Route," *J. Supercrit. Fluids*, **36**(3), pp. 202–215.
- [19] Jung, W. M., Kang, S. H., Kim, W.-S., and Choi, C. K., 2000, "Particle Morphology of Calcium Carbonate Precipitated by Gas–liquid Reaction in a Couette–Taylor Reactor," *Chem. Eng. Sci.*, **55**(4), pp. 733–747.
- [20] Han, Y. S., Hadiko, G., Fuji, M., and Takahashi, M., 2006, "Factors Affecting the Phase and Morphology of CaCO₃ Prepared by a Bubbling Method," *J. Eur. Ceram. Soc.*, **26**(4–5), pp. 843–847.
- [21] Ukrainczyk, M., Kontrec, J., Babić-Ivančić, V., Brečević, L., and Kralj, D., 2007, "Experimental Design Approach to Calcium Carbonate Precipitation in a Semicontinuous Process," *Powder Technol.*, **171**(3), pp. 192–199.
- [22] Wang, H., Huang, W., and Han, Y., 2013, "Diffusion-Reaction Compromise the Polymorphs of Precipitated Calcium Carbonate," *Particuology*, **11**(3), pp. 301–308.
- [23] Sun, Y., Yao, M.-S., Zhang, J.-P., and Yang, G., 2011, "Indirect CO₂ Mineral Sequestration by Steelmaking Slag with NH₄Cl as Leaching Solution," *Chem. Eng. J.*, **173**(2), pp. 437–445.
- [24] Li, G., Li, Z., and Ma, H., 2013, "Synthesis of Aragonite by Carbonization from Dolomite without Any Additives," *Int. J. Miner. Process.*, **123**, pp. 25–31.
- [25] Sundermann, C. M., 2016, "Production of Calcium Carbonate from Steelmaking Slag and Captured CO₂- Optimisation of the Carbonation Process and Product Quality," Aalto University.
- [26] Brecevic, L., and Kralj, D., 2007, "On Calcium Carbonates: From Fundamental Research to Application," *Croat. Chem. ACTA*, **80**.
- [27] García Carmona, J., Gómez Morales, J., and Rodríguez Clemente, R., 2003, "Rhombohedral–scalenoedra Calcite Transition Produced by Adjusting the Solution Electrical Conductivity in the System Ca(OH)₂–CO₂–H₂O," *J. Colloid Interface Sci.*, **261**(2), pp. 434–440.
- [28] Wang, L., Sondi, I., and Matijević, E., 1999, "Preparation of Uniform Needle-Like Aragonite Particles by Homogeneous Precipitation," *J. Colloid Interface Sci.*, **218**(2), pp. 545–553.
- [29] Gómez-Díaz, D., Navaza, J. M., and Sanjurjo, B., 2006, "Analysis of Mass Transfer in the Precipitation Process of Calcium Carbonate Using a Gas/Liquid Reaction," *Chem. Eng. J.*, **116**(3), pp. 203–209.
- [30] Mattila, H.-P., Grigaliūnaitė, I., and Zevenhoven, R., 2012, "Chemical Kinetics Modeling and Process Parameter Sensitivity for Precipitated Calcium Carbonate Production from Steelmaking Slags," *Chem. Eng. J.*, **192**, pp. 77–89.
- [31] Schaschke, C., 2014, *A Dictionary of Chemical Engineering*, Oxford University Press, Oxford.
- [32] Lo, I. M. C., and Lai, K. C. K., 2007, "Redox and Precipitation," *Remediation Technologies for Soils and Groundwater*, American Society of Civil Engineers, Reston, Va., pp. 133–175.
- [33] Čejka, J., Corma, A., and Zones, S., eds., 2010, *Zeolites and Catalysis: Synthesis, Reactions and Applications*, Wiley-VCH, Weinheim.
- [34] Mullin, J. W., 2001, *Crystallization (4th Edition)*, Elsevier.
- [35] Higson, S., 2003, "Analyses Based on Solubility Effects, Precipitation, and the Determination of Mass," *Analytical Chemistry*, Oxford University Press, Oxford ; New York, pp. 93–109.

- [36] Trippa, G., 2006, "Process Intensification of Liquid Phase and Gas-Liquid Precipitation of Calcium Carbonate in Narrow Channel Reactors," University of Newcastle upon Tyne.
- [37] Findlay, A., and Shen, B., 1912, "The Influence of Colloids and Fine Suspensions on the Solubility of Gases in Water. Part II. Solubility of Carbon Dioxide and of Hydrogen," *J. Chem. Soc.*, **101**, pp. 1459–1468.
- [38] Rumpf, B., Nicolaisen, H., and Maurer, G., 1994, "Solubility of Carbon Dioxide in Aqueous Solutions of Ammonium Chloride at Temperatures from 313 K to 433 K and Pressures up to 10 MPa," *Berichte Bunsenges. Für Phys. Chem.*, **98**(8), pp. 1077–1081.
- [39] NIST, 2007, "IUPAC-NIST Solubilities Database" [Online]. Available: https://srdata.nist.gov/solubility/sol_detail.aspx?goBack=Y&sysID=62_92. [Accessed: 07-Nov-2016].
- [40] Trambouze, P., and Euzen, J.-P., 2004, *Chemical Reactors: From Design to Operation*, Editions Technip, Paris.
- [41] NPTEL, 2014, *Mod-01 Lec-20 Gas-Liquid Reactions-1: Theories of Mass Transfer into Agitated Liquids*.
- [42] Roizard, C., and Wild, G., 2002, "Mass Transfer with Chemical Reaction: The Slow Reaction Regime Revisited," *Chem. Eng. Sci.*, **57**(16), pp. 3479–3484.
- [43] Van Elk, E. P., Knaap, M. C., and Versteeg, G. F., 2006, "Application of the Penetration Theory for Gas-Liquid Mass Transfer without Liquid Bulk - Differences with Systems with a Bulk," *ICHEME*, pp. 294–310.
- [44] NPTEL, 2014, *Mod-01 Lec-22 GLR-3: Transition to Fast Reaction, and the Fast Reaction Regime*.
- [45] NPTEL, 2014, *Mod-01 Lec-21 GLR-2: Effect of Chemical Reaction on Mass Transfer: The Slow Reaction Regime*.
- [46] Chen, W.-H., Tsai, M.-H., and Hung, C.-I., 2014, "Characterization of Transient CO₂ Transport in Two Convecting Aerosol Droplets in Tandem," *Aerosol Air Qual. Res.*, **14**, pp. 207–219.
- [47] Chen, W.-H., 2001, "Unsteady Absorption of Sulfur Dioxide by an Atmospheric Water Droplet with Internal Circulation," *Atmos. Environ.*, **35**(13), pp. 2375–2393.
- [48] Elperin, T., and Fominykh, A., 2005, "Conjugate Mass Transfer during Gas Absorption by Falling Liquid Droplet with Internal Circulation," *Atmos. Environ.*, **39**(25), pp. 4575–4582.
- [49] Lu, H.-H., Wu, T.-C., Yang, Y.-M., and Maa, J.-R., 1998, "Transient Heat and Mass Transfer in a Drop Experiencing Absorption with Internal Circulation," *Int. Commun. Heat Mass Transf.*, **25**(8), pp. 1115–1126.
- [50] Ayyaswamy, P. S., Sadhal, S. S., and Huang, L. J., 1990, "Effect of Internal Circulation on the Transport to a Moving Drop," *Int. Commun. Heat Mass Transf.*, **17**(6), pp. 689–702.
- [51] Sirignano, W. A., 1999, *Fluid Dynamics and Transport of Droplets and Sprays*, Cambridge University Press, Cambridge, U.K.
- [52] Bart, H.-J., 2013, *Reactive Extraction*, Springer Science & Business Media.
- [53] Schnebelen, M., Ricaud, M., Jakob, A., Sy, D., and Plasari, E., 2015, "Determination of Crystallization Kinetics and Size Distribution Parameters of Agglomerated Calcium Carbonate Nanoparticles during the Carbonation of a Suspension of Lime," *Sci. Res. Publ. Inc*, **4**(Crystal Structure Theory and Applications), pp. 16–27.
- [54] Liang, Y., Chu, G., Wang, J., Huang, Y., Chen, J., Sun, B., and Shao, L., 2014, "Controllable Preparation of Nano-CaCO₃ in a Microporous Tube-in-Tube Microchannel Reactor," *Chem. Eng. Process. Process Intensif.*, **79**, pp. 34–39.

- [55] Geankoplis, C. J., 1993, *Transport Processes and Unit Operations*, Prentice-Hall Internat, London.
- [56] Han, J., Eimer, D. A., and Melaen, M. C., 2013, "Liquid Phase Mass Transfer Coefficient of Carbon Dioxide Absorption by Water Droplet," *Energy Procedia*, **37**, pp. 1728–1735.
- [57] Bang, J.-H., Song, K., Park, S., Jeon, C., Lee, S.-W., and Kim, W., 2015, "Effects of CO₂ Bubble Size, CO₂ Flow Rate and Calcium Source on the Size and Specific Surface Area of CaCO₃ Particles," *Energies*, **8**(10), pp. 12304–12313.
- [58] Mattila, H.-P., and Zevenhoven, R., 2014, "Design of a Continuous Process Setup for Precipitated Calcium Carbonate Production from Steel Converter Slag," *ChemSusChem*, **7**(3), pp. 903–913.
- [59] Eloneva, S., Puheloinen, E.-M., Kanerva, J., Ekroos, A., Zevenhoven, R., and Fogelholm, C.-J., 2010, "Co-Utilisation of CO₂ and Steelmaking Slags for Production of Pure CaCO₃ – Legislative Issues," *J. Clean. Prod.*, **18**(18), pp. 1833–1839.
- [60] Eloneva, S., Teir, S., Salminen, J., Fogelholm, C.-J., and Zevenhoven, R., 2008, "Steel Converter Slag as a Raw Material for Precipitation of Pure Calcium Carbonate," *Ind. Eng. Chem. Res.*, **47**(18), pp. 7104–7111.
- [61] Eloneva, S., 2010, "Reduction of CO₂ Emissions by Mineral Carbonation: Steelmaking Slags as Rawmaterial with a Pure Calcium Carbonate End Product," Doctoral Dissertation, Aalto University.
- [62] Said, A., Mattila, O., Eloneva, S., and Järvinen, M., 2015, "Enhancement of Calcium Dissolution from Steel Slag by Ultrasound," *Chem. Eng. Process. Process Intensif.*, **89**, pp. 1–8.
- [63] Eloneva, S., Teir, S., Revitzer, H., Salminen, J., Said, A., and Fogelholm, C.-J., 2009, "Reduction of CO₂ Emissions from Steel Plants by Using Steelmaking Slags for Production of Marketable Calcium Carbonate," *Steel Res. Int.*
- [64] Liu, H., 2000, *Science and Engineering of Droplets - Fundamentals and Applications*, William Andrew Publishing/Noyes.
- [65] Javed, K. H., Mahmud, T., and Purba, E., 2006, "Enhancement of Mass Transfer in a Spray Tower Using Swirling Gas Flow," *Chem. Eng. Res. Des.*, **84**(6), pp. 465–477.
- [66] Agrawal, K. S., 2013, "Bubble Dynamics and Interface Phenomenon," *J. Eng. Technol. Res.*, **5**(3), pp. 42–51.
- [67] BETE, 2006, "Flue Gas Desulphurization" [Online]. Available: <http://www.spray-nozzle.co.uk/docs/default-source/default-document-library/flue-gas-desulphurisation-technical-manual.pdf?sfvrsn=2>. [Accessed: 28-Nov-2016].
- [68] Brumbaugh, J. E., 2004, "Chapter 1," *Audel HVAC Fundamentals, Volume 2: Heating System Components, Gas and Oil Burners, and Automatic Controls*, John Wiley & Sons, pp. 32–36.
- [69] MonarchNozzlesIndia, n.d., "Our Site," Monarch Nozzles [Online]. Available: <http://monarchnozzlesindia.com/charts.html>.
- [70] Danfoss, 2003, "Facts Worth Knowing about Oil Nozzles" [Online]. Available: <http://heating.danfoss.com/PCMPDF/DKBP060A802.pdf>. [Accessed: 27-Jan-2017].
- [71] Spraying Systems Co., 2015, "Industrial Hydraulic Spray Products."
- [72] Neutrium, 2013, "Terminal Velocity of Particles for Gravity Separation" [Online]. Available: <https://neutrium.net/unit-operations/terminal-velocity-of-particles-for-gravity-separation/>. [Accessed: 13-Dec-2016].
- [73] Clift, R., Grace, J. R., and Weber, M. E., 1978, *Bubbles, Drops, and Particles*, Academic Press, New York.

- [74] Choi, M., Cho, M., and Lee, J. W., 2016, "Empirical Formula for the Mass Flux in Chemical Absorption of CO₂ with Ammonia Droplets," *Appl. Energy*, **164**, pp. 1–9.
- [75] Ali, M., Mahmud, T., Heggs, P., Ghadiri, M., Bayly, A., Crosby, M., Ahmadian, H., Martindejuan, L., and Alam, Z., 2017, "Residence Time Distribution of Glass Ballotini in Isothermal Swirling Flows in a Counter-Current Spray Drying Tower," *Powder Technol.*, **305**, pp. 809–815.
- [76] Anandharamakrishnan, C., 2013, "Computational Fluid Dynamics Applications in Spray Drying of Food Products," *Computational Fluid Dynamics Applications in Food Processing*, Springer, New York, p. 18.
- [77] Malvern Instruments Ltd, 1991, "Instruction Manual - System 2600."

Appendices

Appendix A – Results of the Spray Nozzle Analysis (3 pages)

Appendix B – Temperature and pH Recordings of Spray Carbonation Experiments
(2 pages)

Appendix C – Results of the PSD Measurements (1 page)

Appendix A – Results of the Spray Nozzle Analysis

All measurement data obtained during the spray nozzle analysis with Malvern particle sizer can be found from the following table.

	Rec. No	Pressure [bar]	N-L-D ¹ [cm]	Temp. [°C]	D[3,2] – Surface weighted mean	D(v, 0.1) [µm]	D(v, 0.5) [µm]	D(v, 0.9) [µm]
Monarch 5.50 GPH 60° PLP	1	4.00	2	22.2	54.32	29.46	93.75	175.52
	2	4.00	2	22.2	54.36	29.47	93.68	175.83
	3	3.15	2	22.7	57.63	33.09	100.75	185.29
	4	3.15	2	22.8	56.88	32.51	100.31	184.65
	5	2.60	2	22.7	63.73	36.79	107.56	199.11
	6	2.60	2	22.6	63.76	36.85	107.57	199.42
	7	1.80	2	22.6	85.56	50.72	133.41	243.22
	8	1.80	2	22.6	84.27	48.94	132.59	238.34
	9	4.00	2	22.5	53.03	27.85	92.29	185.21
	10	4.90	4	22.3	44.29	23.72	73.73	155.76
	11	4.90	4	22.3	44.43	23.63	73.78	158.19
	12	4.00	4	22.3	49.96	26.70	84.13	175.94
	13	3.10	4	22.4	55.89	31.28	96.53	192.37
	14	2.50	4	22.4	65.72	35.84	108.69	208.93
	15	1.70	4	22.4	100.32	56.36	160.00	276.86
	16	4.00	4	22.4	50.58	27.11	85.75	185.09
	17	5.00	4	22.4	47.16	24.84	81.14	192.51
	18	4.90	4	22.4	47.32	25.01	81.84	194.24
	19	4.90	4	22.5	46.56	24.75	79.27	158.95
	20	4.00	4	22.6	52.44	27.89	88.82	176.15
	21	3.00	4	22.7	58.47	32.01	98.59	186.98
	22	2.60	4	22.7	65.74	36.29	106.49	197.04
	23	5.00	4	22.9	51.55	26.98	88.86	179.19
	24	4.90	4	22.9	53.07	27.71	90.99	184.03
	25	5.00	2	22.5	59.76	34.21	101.89	195.19
	26	5.00	2	22.2	60.15	34.80	102.77	195.06
	27	5.00	2	22.1	60.16	34.44	102.36	194.93
	28	5.00	2	22.3	60.25	34.37	102.34	196.12
	29	4.00	2	22.7	62.11	35.96	105.01	198.31
	30	4.00	2	22.7	56.38	33.00	98.39	185.55
	31	4.00	2	22.9	59.83	34.74	102.20	193.09
	32	4.00	2	23.0	60.67	35.24	103.32	195.89
	33	3.00	2	23.1	67.38	39.74	111.11	207.85
	34	3.00	2	23.1	64.80	38.28	108.26	201.93
	35	3.00	2	23.0	65.65	38.83	109.35	204.61
	36	2.60	2	22.9	71.63	42.61	116.56	214.76
	37	2.60	2	22.9	71.75	42.57	116.52	214.13

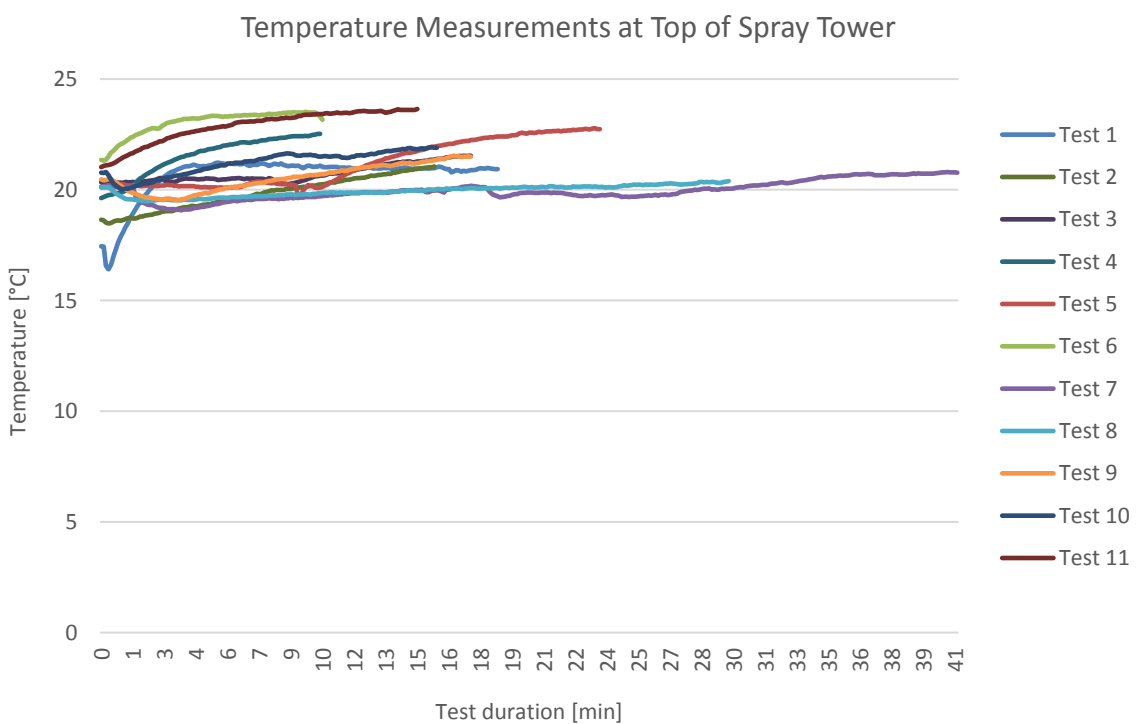
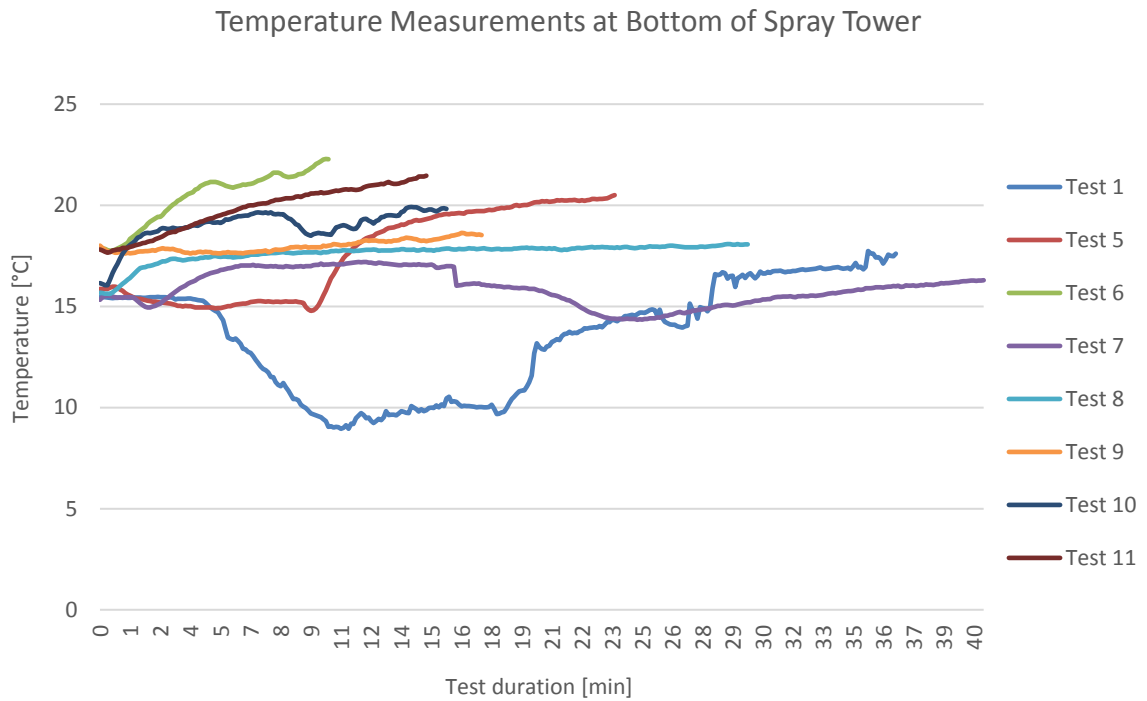
¹ N-L-D = Nozzle-to-lazer beam distance

	Rec. No	Pressure [bar]	N-L-D [cm]	Temp. [°C]	D[3,2] – Surface weighted mean	D(v, 0.1) [µm]	D(v, 0.5) [µm]	D(v, 0.9) [µm]
Monarch 0.60 GPH 45° R	38	5.20	4	22.4	51.97	29.19	70.64	135.22
	39	5.20	4	22.1	51.62	28.94	70.33	135.52
	40	5.00	4	22.2	49.91	29.16	72.59	125.60
	41	5.00	4	22.1	52.54	29.07	73.92	135.41
	42	5.00	4	22.1	52.88	29.38	74.02	136.00
	43	5.00	4	22.1	52.18	28.91	73.66	140.98
	44	5.00	4	22.1	47.79	27.93	64.05	113.26
	45	4.50	4	22.1	55.68	30.48	79.90	152.03
	46	4.50	4	22.1	52.18	30.36	79.37	140.93
	47	4.50	4	22.1	53.14	30.80	80.14	142.19
	48	4.50	4	22.1	55.85	30.37	80.06	154.01
	49	5.20	4	22.1	47.72	28.57	64.15	106.59
	50	5.20	4	22.1	47.92	28.80	64.25	107.20
DANFOSS 5.50 GPH 45° S	51	5.00	4	21.2	59.33	30.78	97.60	192.74
	52	5.00	4	21.2	58.70	30.41	96.17	190.78
	53	5.00	4	21.1	58.24	30.14	95.27	189.50
	54	5.00	4	21.2	57.00	29.53	92.97	187.00
	55	4.00	4	21.6	62.76	33.10	99.98	192.09
	56	4.00	4	21.7	62.82	33.25	100.29	191.38
	57	4.00	4	21.7	62.49	32.98	99.91	190.77
	58	4.00	4	21.6	62.71	33.14	100.40	192.02
	59	3.00	4	21.5	79.69	42.21	125.14	221.00
	60	3.00	4	21.5	79.81	42.36	125.24	221.31
	61	3.00	4	21.6	79.97	42.58	125.64	220.52
	62	2.40	4	21.5	97.61	53.03	153.79	256.69
	63	2.40	4	21.5	98.11	53.47	154.65	257.72
	64	2.40	4	21.5	99.03	53.96	155.49	259.86
Monarch 5.50 GPH 30° HV	65	5.00	4	21.5	41.72	23.44	66.43	135.95
	66	5.00	4	21.4	41.45	23.23	66.21	135.05
	67	5.00	4	21.4	40.66	23.16	62.54	129.14
	68	5.00	4	21.4	40.34	23.08	61.22	126.51
	69	4.00	4	21.3	48.39	26.96	76.17	147.09
	70	4.00	4	21.4	48.50	27.02	76.40	147.93
	71	4.00	4	21.4	48.89	27.09	77.28	150.69
	72	4.00	4	21.4	49.11	27.19	77.66	151.74
	73	2.90	4	21.4	74.63	40.68	117.45	213.05
	74	2.90	4	21.4	74.97	40.87	118.17	214.33
	75	2.90	4	21.4	75.63	41.23	119.17	215.14
	76	2.60	4	21.3	84.95	46.11	134.33	238.00
	77	2.60	4	21.4	84.76	45.94	133.75	237.97
	78	2.60	4	21.4	84.75	46.05	133.83	238.56
DANFOSS 0.60 GPH 45°	79	5.00	4	21.6	43.92	24.76	60.27	110.37
	80	5.00	4	21.5	44.99	25.21	61.80	113.64
	81	5.00	4	21.5	45.20	25.28	62.30	114.47
	82	5.00	4	21.5	45.14	26.30	63.06	103.90
	83	4.20	4	21.9	50.35	27.78	74.72	129.31
	84	4.20	4	21.7	51.34	27.87	76.33	134.08
	85	4.00	4	21.7	54.34	28.81	81.60	146.54
	86	3.85	4	21.7	55.77	29.27	84.10	154.12

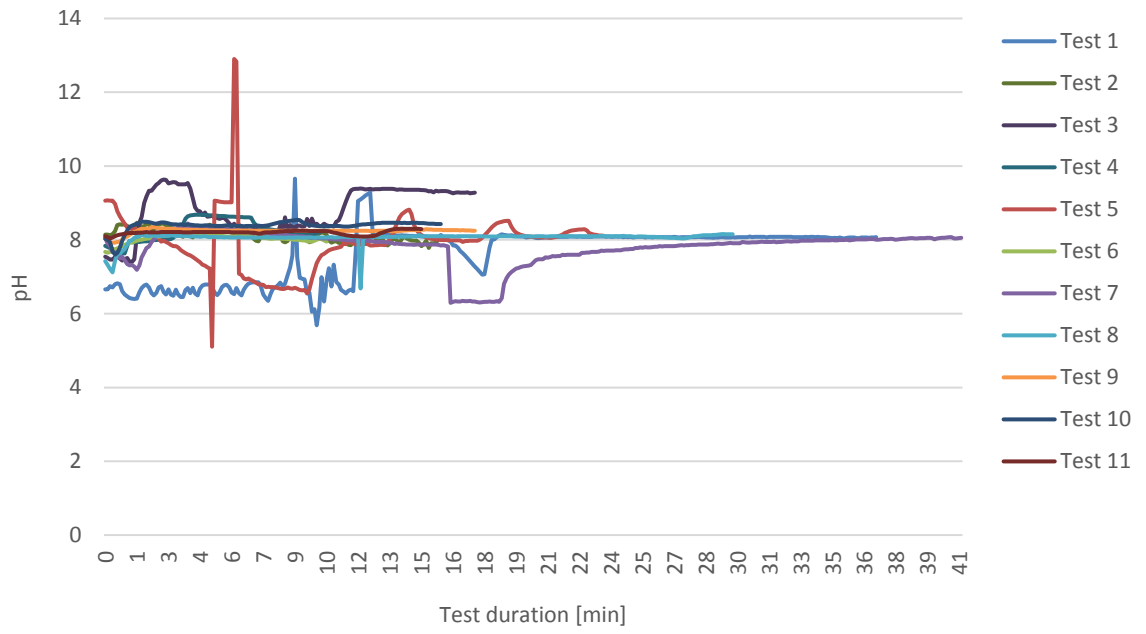
	Rec. No	Pressure [bar]	N-L-D [cm]	Temp. [°C]	D[3,2] – Surface weighted mean	D(v, 0.1) [µm]	D(v, 0.5) [µm]	D(v, 0.9) [µm]
DANFOSS 1.50 GPH 45°	87	5.00	4	21.6	43.92	25.21	66.76	118.28
	88	5.00	4	21.6	43.16	25.28	66.38	112.83
	89	5.00	4	21.5	43.37	25.30	66.33	113.41
	90	5.00	4	21.5	43.20	25.32	66.16	113.19
	91	4.00	4	21.5	53.60	30.41	85.99	146.98
	92	4.00	4	21.5	53.83	30.45	85.59	146.14
	93	4.00	4	21.5	53.83	30.35	85.82	146.98
	94	4.00	4	21.4	54.86	30.52	85.95	147.01
	95	3.00	4	21.5	67.88	36.68	118.63	201.00
	96	3.00	4	21.5	70.21	36.45	114.37	193.66
	97	3.00	4	21.5	73.30	37.00	116.97	197.61
	98	2.50	4	21.4	85.97	40.68	136.78	228.07
	99	2.50	4	21.4	86.84	40.68	136.90	229.06
100	2.50	4	21.4	87.03	40.99	137.22	228.44	
DANFOSS 2.50 GPH 45°	101	5.00	4	21.1	48.47	26.82	76.34	133.25
	102	5.00	4	21.0	48.21	26.69	76.08	132.95
	103	5.00	4	21.1	47.84	26.58	75.91	132.70
	104	5.00	4	21.2	47.24	26.50	75.85	132.42
	105	4.00	4	21.1	57.89	31.89	93.88	166.36
	106	4.00	4	21.0	58.03	33.47	97.07	167.64
	107	4.00	4	20.9	57.52	33.30	96.89	167.39
	108	4.00	4	20.8	58.92	33.45	96.73	166.92
	109	3.00	4	20.9	89.61	48.01	137.99	225.01
	110	3.00	4	20.8	84.32	45.15	129.70	215.62
	111	3.00	4	20.9	85.05	45.57	130.64	216.13
	112	2.40	4	20.9	107.19	57.84	167.02	277.30
	113	2.60	4	21.1	92.66	46.49	143.26	233.67
	114	2.60	4	21.2	92.85	46.84	143.79	235.12

Appendix B – Temperature and pH Recordings of Spray Carbonation Experiments

The temperature and pH measurements recorded during the spray carbonation experiments are presented in the following charts.



pH Measurements at Bottom of Spray Tower



Appendix C – Results of the PSD Measurements

All Measurement data obtained from the particle size distribution analysis with Malvern Mastersizer 2000 are summarized in the following table:

		D [4,3] – Volume weighted mean	D[3,2] – Surface weighted mean	D(v, 0.1) [µm]	D(v, 0.5) [µm]	D(v, 0.9) [µm]
Test1	no us	47.23	32.51	18.47	36.21	82.86
	us on	36.88	27.50	16.38	29.93	61.41
	us off	36.64	27.36	16.32	29.77	60.84
Test2	no us	35.54	8.54	10.52	22.86	52.25
	us on	31.99	7.77	9.70	20.68	44.77
	us off	35.53	8.05	9.88	21.24	53.23
Test3	no us	75.40	14.38	13.69	42.56	189.23
	us on	33.85	10.15	11.14	29.05	64.46
	us off	39.70	10.43	11.39	29.61	71.47
Test4	no us	36.23	27.44	18.82	33.66	58.18
	us on	30.74	23.79	17.55	29.13	47.05
	us off	37.04	24.45	17.64	29.50	50.03
Test5	no us	47.10	40.02	25.33	43.44	74.65
	us on	40.83	36.39	24.63	38.57	60.43
	us off	40.46	36.10	24.48	38.25	59.78
Test6	no us	79.74	43.88	26.71	46.15	93.12
	us on	52.19	38.01	24.20	40.11	70.80
	us off	51.38	37.80	24.11	39.91	70.17
Test7	no us	45.47	16.70	13.75	29.29	63.02
	us on	26.60	8.62	10.96	24.41	46.35
	us off	35.64	21.33	13.04	25.90	53.15
Test8	no us	135.09	25.19	24.47	66.98	352.10
	us on	105.85	20.59	21.14	55.50	251.05
	us off	86.68	23.80	21.04	53.33	184.12
Test9	no us	97.83	21.64	24.93	53.70	124.08
	us on	56.69	26.73	22.02	43.20	86.03
	us off	52.78	35.62	22.22	42.28	81.75
Test10	no us	51.53	39.31	27.31	47.86	82.08
	us on	43.76	34.34	25.60	41.74	66.05
	us off	43.41	34.12	25.46	41.41	65.45
Test11	no us	65.62	47.69	30.67	57.55	106.11
	us on	52.65	43.94	27.34	47.96	84.87
	us off	51.36	43.34	27.33	47.06	81.70